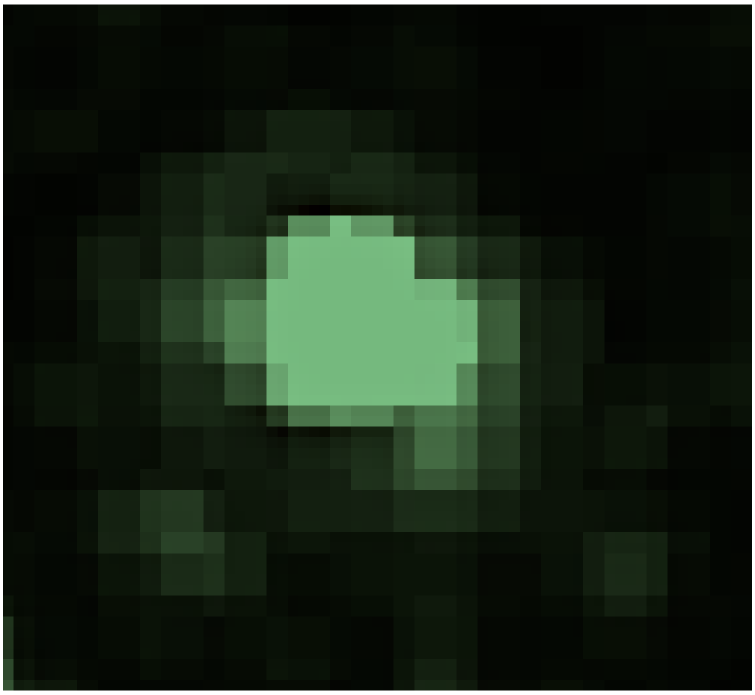

Protein corona formation and structural changes of lipid nanoparticles investigated using QCM-D and waveguide microscopy

Master's thesis in Physics

SARA MOHAMMADI

DEPARTMENT OF PHYSICS

CHALMERS UNIVERSITY OF TECHNOLOGY
Gothenburg, Sweden 2021
www.chalmers.se

Master's thesis 2021

Protein corona formation and structural changes of lipid nanoparticles investigated using QCM-D and waveguide microscopy

SARA MOHAMMADI

Department of PHYSICS
Division of Nano and Biophysics
Chalmers University of Technology
Gothenburg, Sweden 2021

Protein corona formation and structural changes of lipid nanoparticles investigated using QCM-D and waveguide microscopy

Sara Mohammadi

Supervisor: Fredrik Höök, Mattias Sjöberg and Björn Agnarsson, Department of physics
Examiner: Fredrik Höök, Department of physics

Master's Thesis 2021
Department of physics
Division of Nano and Biophysics
Chalmers University of Technology
SE-412 96 Gothenburg
Telephone +46 31 772 1000

Cover: By zooming in on a single lipid nanoparticle image taken with waveguide microscopy with scattering mode at wavelength 532 nm; one can see the heart of the lipid nanoparticle.

Typeset in LaTeX
Printed by Chalmers Reproservice
Gothenburg, Sweden 2021

Protein corona formation and structural changes of lipid nanoparticles investigated using QCM-D and waveguide microscopy
SARA MOHAMMADI
Department of Physics
Chalmers University of Technology

Abstract

Lipid nanoparticles (LNPs) are being increasingly considered for use in drug delivery. However, understanding the interactions of LNPs with a biological environment is crucial for successful deliver of their cargo, such as for example mRNA, across cellular membranes. Upon exposure to a biological fluid it is believed that the surface of LNPs is spontaneously covered by a protein corona, a layer of adhered biomolecules, prior to being taken up by the targeted cells. A protein of interest in this context is Apolipoprotein-E (ApoE), both because it is known to be part of the protein corona and because it may control endocytic uptake via specific interactions with receptors in the cell membrane. Furthermore, ApoE-coated LNPs are expected to undergo a structural change in the acidic environment of the endosome during cargo release to the cytosol.

In this master thesis, we have studied protein-corona formation and the reaction of the LNPs covered/not covered with ApoE in an acid environment that mimics the endosomal environment using label-free surface-based bioanalytical tools such as quartz crystal microbalance with dissipation monitoring (QCM-D) and waveguide microscopy. QCM-D provides information based on ensemble averaging of the biological interactions taking place on the surface of the sensor, while waveguide microscopy provides both ensemble-averaged data and information based on inspection of individual LNPs. Further, waveguide microscopy is capable of detecting both light scattering and fluorescence signals, which provides the possibility to observe both the labeled interior of the LNPs and binding of unlabeled protein.

We found that ApoE bind to PEG-modified LNPs with a lag-time of tens of minutes unless mixed with bovine serum albumin (BSA). This is attributed to BSA-induced PEG shedding which promotes ApoE binding. Inspections using combined label-free and fluorescence based waveguide microscopy releveled a weaker than expected dependence between cargo fluorescence and scattering intensity, suggesting that the self-assembly process utilized for LNP fabrication may vary with LNP size. It is also concluded that further liquid handling must be improved to follow ApoE binding to LNPs using waveguide microscopy.

Keywords: Waveguide microscopy, Quartz crystal microbalance with dissipation monitoring, label-free, apolipoprotein-E, corona formation, protein corona, lipid nanoparticle, MC3, drug delivery, mRNA therapy, serum protein, endosomal membrane.

Acknowledgements

I would like to express my gratitude to everyone who helped during this fantastic master's thesis journey.

Peter Apell. Thank you for introducing me to the field of biological physics and Fredrik Höök.

Fredrik Höök, both supervisor and examiner. Thank you for both giving me the opportunity to work on this project, in which the subject of this thesis is close to my heart, and for having the pleasure of being a project supervisor in one of your master courses. Furthermore, giving me the opportunity to work with beautiful people among others, Mattias Sjöberg and Björn Agnarsson.

Mattias Sjöberg, my first supervisor. Words can not describe my gratitude to you. Thank you for everything. Thank you for being an excellent supervisor and colleague to me. Thank you that the door to your office was always open whenever I ran into a trouble spot or had a question. I am really surprised by your way of supervising, taking care of your students and your sense of humor.

Björn Agnarsson, my second supervisor. Thank you for always being helpful and kind to me. I really enjoyed our waveguide experiments, discussions, and all the sound effects that I have learned from you.

I would like also to thank you **Adrián González Rodríguez**, **Erik Olsén** and **Nima Aliakbari**, for all the interesting discussions, both work and not work-related.

In the end, thank you all in the **Nano and Biophysics** for a very open and friendly environment, with very interesting discussions during our lunch and fika breaks.

A final special thanks go to my family and friends, especially to **my parents**, who made much effort to make the possibility for me to get the opportunity to study.

Sara Mohammadi, Gothenburg, May 2021

Contents

List of Figures

List of Tables

1

Introduction

Nucleotide-based therapies have recently attracted increased attention due to their potential to prevent and treat many presently untreatable diseases [1][2][3] such as Alzheimer's[4][5], diabetes[6], and cardiovascular diseases[7]. A striking example of their potential is the mRNA-based Covid-19 vaccines produced by for example Pfizer and Moderna, which appear promising in the globe strive to curb the current pandemic[8].

However, to fully utilize the broad potential of this novel approach beyond vaccines and to improve the latter, there is a need for understanding the mechanisms behind cellular uptake of the nucleotide-based formulation. For example, how should one deliver nucleotide-containing nanocarriers to the target cells of interest and how should the interactions be steered to ensure efficient uptake? Further, once taken up by a cell, how is the nucleotide content released for efficient translation into proteins that the body is missing? [9].

In the following sections, a background to these questions are provided, aiming to motivate the work of the thesis and provide the information needed to follow the subsequent sections.

1.1 Background

Efficient delivery of nucleotide-based therapies such as DNA and RNA is a key challenge, since these can not penetrate the cell membrane by themselves. DNA and RNA carry electric charge, and are thus blocked by the cell membrane that acts a barrier which separates the internal and the external environment of the cell from each other. Because of this, these therapeutic nucleotides need to be packed in nanocarriers, often called biological nanoparticles (BNPs), to be transported to and into a target cell.

An important phenomenon which impacts the fate of BNPs is the so-called protein corona formation, which occurs spontaneously on the surface of BNPs prior to cellular uptake. The protein corona is a layer of proteins that forms at the surface of the BNPs. Once the corona formation has occurred, the BNPs are believed to be taken up via specific interactions with receptors present in the cell membrane [10].

There are also several other factors that play a role in uptake or internalization of

BNPs such as chemical composition, surface charge, shape and size. BNPs with a diameter around 100 nm are believed to have a higher probability of being taken up by the cell [11]. Once the BNPs are taken up by the cell, the BNPs get enclosed by cell membrane and ends up in the, so-called endosome. Inside the endosome the pH value starts to decrease, which causes structural changes in the BNPs. This structural changes of the BNPs lead to fusion with the endosomal membrane and release of their cargo into the so-called cytosol of the cell[12].

This thesis focuses on BNPs containing mRNA due to its high potential in therapeutic applications in comparison to DNA which carries additional challenges [13]. Some advantages of mRNA are that it is highly selective and contains only a specific genetic code for a specific protein that the body is missing, and it can be translated by the ribosomes that are present in the cytosol. This means the mRNA does not interact with the cell nucleus, unlike DNA that requires nuclear entery[13][14]. Therefore, mRNA-based nucleotide based therapy is less challenging than DNA therapy. Moreover, after the mRNA is translated to protein by the ribosome, it is degraded through the physiological pathways [14].

1.2 Lipid nanoparticles

One of the significant difficulties in nano-drug treatments is the poor degree of penetration of the BNPs into the cell and the release of its cargo. However, despite recent progress in this field, there are still many challenges to overcome. These challanges include having a sophisticated nano-carrier that is biocompatible with negatively charged naked mRNA while also enable release of the mRNA furher the BNPs can travel in the blood; for a longer time before it gets degraded by unwanted enzymes or uptaken by other untargeted cells [15].

The lipid nanoparticles (LNP) system is currently a promising candidate system for genetic therapy delivery system. The origin of the LNP idea comes from observing natural biological nanoparticles, e.g. exosomes, which are used as a delivery system for both small and larger molecules by the body itself [11].

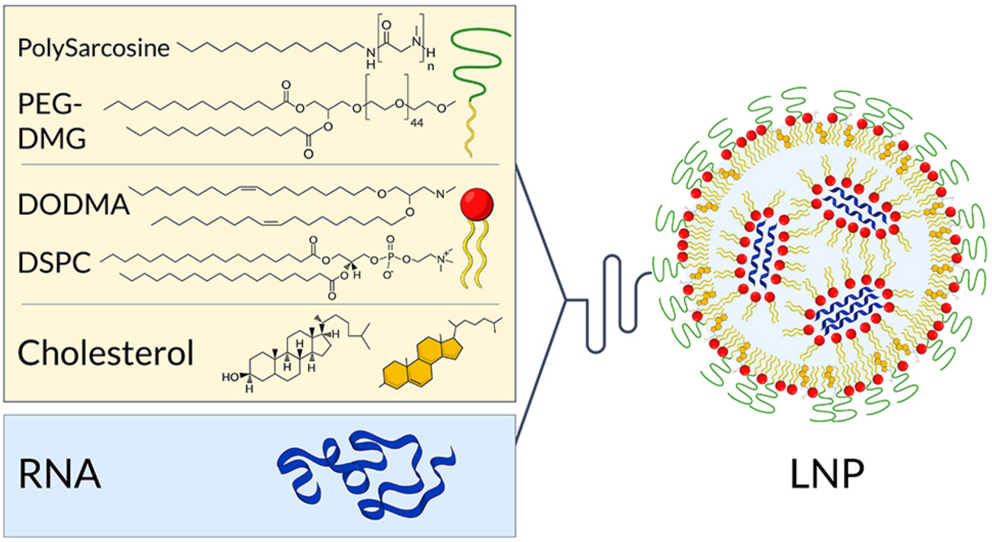

Figure 1.1: A quite similar model of a lipid nanoparticle (LNP) containg cargo (mRNA) which is enclosed by cationic lipds. The outer shell of the LNP is covered by the PEG-lipids. The image is reproduced from Osborn, Dr. Rae. "Difference Between mRNA Vaccine and Traditional Vaccine." Difference Between Similar Terms and Objects, 21 December, 2020[16] under CC BY-NC-ND 4.0 licence.

These LNPs have proven helpful for drug delivery applications [11]. They have a monolayer of lipids on their surface that acts as a barrier and separates the interior of the vesicle from the exterior. In this work, the LNPs contains O-(Z,Z,Z,1Z-heptatriacont-6,9,26,29-tetraene-19-yl)-4-(N,N-dimethylamino)butanoate- (Dlin-MC3-DMA), which is a cationic lipid having a dissociation constant (pKa) of 6.44, used to encapsulate mRNA due to strong electrostatic interaction. For further details of the LNP production, the reader is encouraged to read[11].

Additionally, when Dlin-MC3-DMA is in an environment where the pH value is below its pKa, like inside the endosome, the ionizable lipid gets protonated. It then interacts with the anionic endosomal lipids, leading to the release of the cargo into the cytosol, which will further be translated to the desired protein by ribosomes in the cytosol[11].

Along with Dlin-MC3-DMA, there are other lipids contained in the LNP such as distearoylphosphatidlycholine-(DSPC), biotin-lipid, cholesterol, 1,2-Dimyristoyl-sn-Glycero-3-Phosphoethanolamine (DMPE), conjugated Polyethylene Glycol- (DMPE PEG), rhodamine and PEGylated phospholipid—a polyethylene glycol (PEG-lipids) which is an inert, biocompatible polymer that are covalently attached to the headgroup of a phospholipid [11].

One of the most important roles of the PEG, besides preventing aggregation of the LNPs with each other or with the different environment analytes (protein serum), is also that it shields LNPs both from enzymes and other cells that are not the target cell, which lead to increasing bloodstream circulation lifetime of the LNPs [11]. In addition, LNPs lose their PEG-lipids upon interacting with the serum proteins over time, in a process called PEG-shedding. Figure (1.1), a cartoon of LNP mimics is illustrated, which is quite similar to the LNPs described here [11].

1.3 Protein corona

Blood plasma, the liquid component of blood in which the blood cells are suspended, contains several different proteins of different concentrations [17]. When nanoparticles (NPs), e.g. nanocarriers, are transferred inside the blood, many of these proteins attach to the surface of the NP, forming a layer of proteins referred to as the protein corona. In the beginning, the most abundant proteins are adsorbed on the surface, known as the soft corona. After a while, these proteins are substituted by proteins with a higher affinity but lower concentration and forms the hard corona[18].

The composition and structure of the protein corona depend on many factors of the NPs such as size, curvature, surface charge, body temperature and shape of the NPs, as well as duration of exposure. Thus, the composition of each corona is different since it depends on many parameters. Once a corona formation has occurred, it gives the NPs a new biological identity, which helps the NPs to be seen and taken up by the cells [11].

The composition of the corona has been studied with different methods such as dynamic light scattering or differential centrifugal sedimentation, and it has been found that proteins of a slight negative charge, such as albumin and apolipoproteins play an important role in the protein corona. These proteins show an affinity for hydrophobic surfaces [18][19], and as soon the hydrophobicity of an NP surface decreases, fewer apolipoproteins adsorb[19].

The binding of proteins to NPs may cause protein structural rearrangements that are thermodynamically is favorable. These changes are typically irreversible even after desorption from the NP. The larger the curvature of the NPs compared with the size of the proteins the more are the proteins believed to retain their original structure after binding. However, different studies indicate that the perturbation of protein structure may occur [10].

1.3.1 Apolipoprotein-E

Apolipoprotein-E (ApoE) is one of the serum proteins present in the bloodstream that has an important role in the corona formation[17]. ApoE concentration is ca. 3-7 mg/dl in an adult [20] and it has its isoelectric point (pKa) at 5.65[21]. ApoE binds to the surface of BNPs and acts as "address tags," and determines the destination of the BNPs. Furthermore, ApoE binds to the cell via the so-called low-density lipoprotein (LDL) ligand. LDL ligand is a common receptor that is present on the surface of all types of cells. The amount of LDL receptor varies, depending on the type of cell we are looking at [22][23].

ApoE is an amphiphatic protein, which means that it contains both polar (hydrophilic property) and nonpolar (hydrophobic property) regions. ApoE binds to the cell membrane with its C-terminal (hydrophilic property) to the N-terminal of the LDL-receptors. ApoE is composed of 299 amino acids and has a molecular weight of 34 kDa. ApoE is polymorphic with three dominant alleles: ApoE2, ApoE3, and ApoE4. Usually, a healthy person has two of the three alleles. Those with ApoE4 are recognized as having a higher risk for the cascade of Alzheimer's than those who do not carry these genes due to ApoE4 associated with the increased risk for the cerebral amyloidal. Unlike ApoE4, ApoE2 gives more of a genetic defense to neuro-degeneration diseases and lowers the risk [23][22].

In this work, ApoE3 is used because it is the most common allele and it has been shown that ApoE3 has a significant role in the protein corona formation and endocytic uptake via specific interactions with receptors in the cell membrane[10].

1.3.2 Albumin

Albumin is the most abundant protein in the serum in the blood,[10][24]. It is a water-soluble and composed of 585 amino acids and has molecular weight of 66.5 kDa. Albumin has a pKa at 4.9 [25]. It has many functions, among others, to transport various hydrophobic macromolecules such as fatty acids, drugs, and hormones to a target cell in an aqueous environment [10]. Here bovine serum albumin is used to speed up PEG-shedding of the LNPs which furthere will increase the binding of ApoE to LNPs.

1.4 Endosomal pathway

Once corona formation has occurred, the LNPs get internalized through the cell membrane and ends up in an endosome inside the cell, where the LNPs will get either degraded or deliver its nucleotide cargo into the cytosol. This pathway is called the endocytosis pathway [26][12]. Inside of the endosome, the pH value decreases gradually[26]. At the beginning when the pH starts to become slightly acidic is called early endosomes and acts as a sorting station. It is expected that the LNPs that contain MC3 releases their cargo at the early endosome stage[11].

When a cargo is not released from the early endosome, the pH continues to decrease down to 4.6 which defines the so-called late endosome stage. At this point the highly acidic environment and some specific enzymes that are activated at this pH degrade the cargo [27]. Thus, today only a percent of LNPs taken up into cells are then translated into protein[12].

Today many scientists are focusing on enhancing this endosomal escape process, for example by optimizing the LNP design[12].

1.5 Aim of the project

The main aim of this master's thesis has been to find a suitable surface chemistry for binding LNPs while being inert to varying pH, to observe corona formation by ApoE and structural changes of the bare and protein covered LNPs using Quartz crystal microbalance with dissipation monitoring[28] and waveguide microscopy[29].

We hypothesise that ApoE will bind to LNPs after PEG-shedding occurs. Moreover, rinsing LNP with albumin may speed up PEG-shedding and promote ApoE binding. Further, we hypothesise that by decreasing the pH, we should be able to observe some structural changes of LNPs and it is expected to occur after the pH value 6.44, since MC3 in the LNPs start to protonate at this pH value.

2

Methods & Material

In this chapter, the main experimental methods and materials used in this thesis are presented. In Section 2.1, the fundamental principles and setup of QCM-D are described. In the following section, which is Section 2.2, the working principle and setups of waveguide microscopy are described. In Section 2.3, describes the NTA method, which is used for both concentration and size characterization of the LNPs. In the remaining sections, the main materials that have been used in this work is described.

2.1 Quartz crystal microbalance with dissipation monitoring

Quartz crystal microbalance with dissipation monitoring (QCM-D) is a label-free ensemble average nano-sensor which is widely used for biosensing applications [30][31], such as studying protein interactions [32], biopolymers, artificial cells [33] and to study viscoelastic properties of absorbed entities on the surface of the sensor [34].

The main working principle of QDM-D is based on the piezoelectric property of crystalline quartz. The piezoelectric effect is obtained when a quartz crystal at AT-cut, i.e. at an angle 35.35 to its optical axis, is exposed to an external voltage that induces a shear mode oscillation. Consequently, an acoustic wave is propagating perpendicular to the surface is created. The standing wave has a set of resonance frequencies (f_n) when the odd integer number (n) of half-wavelength of the resonance frequency matches the crystal thickness, d_i.

$$f_n = \frac{nv_i}{2d_i} = \frac{nv_i}{\lambda}, \tag{2.1}$$

Where v_i is the speed of propagation of sound in the quartz crystal and λ is the induced acoustic wavelength. A frequency of 5 MHz corresponds to a thickness of 0.33 mm[30]. According to the Sauerbrey equation (2.2)[35], it is possible to convert the frequency shift from the absorption of an entity on the QCM-D sensor to its mass

$$\Delta m = -\frac{S\Delta f_n}{n}, \tag{2.2}$$

where Δf is the change in frequency, Δm is the mass of the adsorbed entity on the sensor, and S is the Sauerbery constant that corresponds to 17.7 ng/Hz cm^2 at resonance frequency 5 MHz, under the assumption that the absorbed mass is thin, rigid, and uniform on the surface [30]. It is worth mentioning that one should be aware of this interpretation of the biomaterial mass from a QCM-D measurement overestimates the mass of the bound entity on the surface sensor since it includes the mass of the bound water molecules to the target entity [36].

In addition to measuring mass adhered to the sensor surface, a QCM-D can also be used to monitor the viscoelastic properties, such as how soft or rigidly an entity is bound to the surface. This is studied by measuring how fast energy dissipates over the time. A rigid body usually has a rapid decrease in dissipation energy than the soft one. In this work, QCM-D in which has been developed by the examiner of this thesis is utilized using the third harmonic, n=3.

2.1.1 QCM-D setups and experimental

QCM-D setups. Figure (2.1a) shows an image of the QCM-D instrument utilized in our work. It consists of a pump and four parallel flow cells, which make possible to perform four simultaneous experiments with a continuous flow rate. The sample solution (PLL-g-PEG-biotin or SLB, SA, LNPs, then proteins) were injected from one side and then discarded from the other side with a constant flow. Figure (2.2a) shows a QCM-D sensor having gold-electrodes and silicon dioxide (SiO_2) as a coating layer where the biological materials are deposited.

Figure 2.1: A photo of a QCM-D instrument with its flow cells and pump.

QCM-D sensor surface cleaning. Prior to the experiments, the sensors were cleaned with Sodium Dodecyl Sulfate (SDS) soap and followed by rinsing with the MilliQ water. MilliQ water is highly purified from organic and inorganic materials and often used for research applications. After a sensor had been washed properly, it was dried with N2 gas. Moreover, the sensor put in a plasma machine cleaner for 40 minutes in order to further clean the surface. The plasma machine

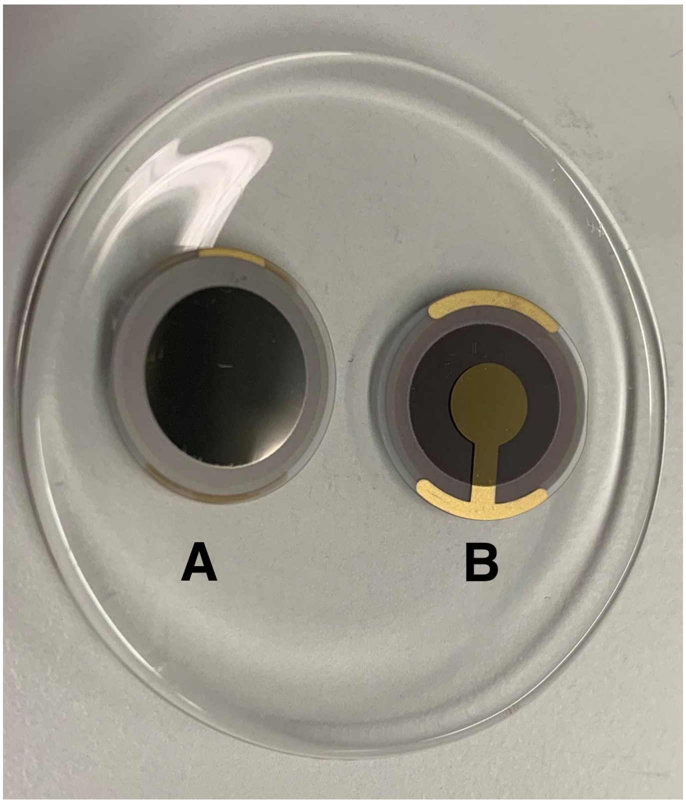

Figure 2.2: QCM-D sensors. The sensor to the left(A) is the SiO_2 coated layer where the biological materials are deposit on and the sensor to the right (B) shows the under of the sensor with gold-electrodes.

cleaner was also used in order to activate the sensor surface to promote biomaterials binding on it.

LNPs and ApoE concentrations used in the QCM-D. As mentioned above, QCM-D provides information based on ensemble averaging of the biological interactions taking place on the surface of the sensor. Therefore QCM-D requires a lot of material to produce its signal. The two most important and expensive materials used in this work are LNPs (obtained from the industrial research center FoRmulaEx) and ApoE (purchased from Sigma). The concentration of the LNPs that was used in the QCM-D measurements was ca. $4x10^{10}$ mL^{-1}. Initially, a ApoE concentration of 5-10g mL^{-1} was used but did not giva a significant signal. Therefore, the concentration of ApoE has increased to 25g mL^{-1} or 735 nM. This amount of the concentration is also close to was ApoE concentration present in our blood serum. Note that all the ApoE addition to the pre-bound LNPs required a continuous flow rate. Therefore, the flow rate of ca. 7 μl min^{-1} was chosen in order to lower the ApoE consumption.

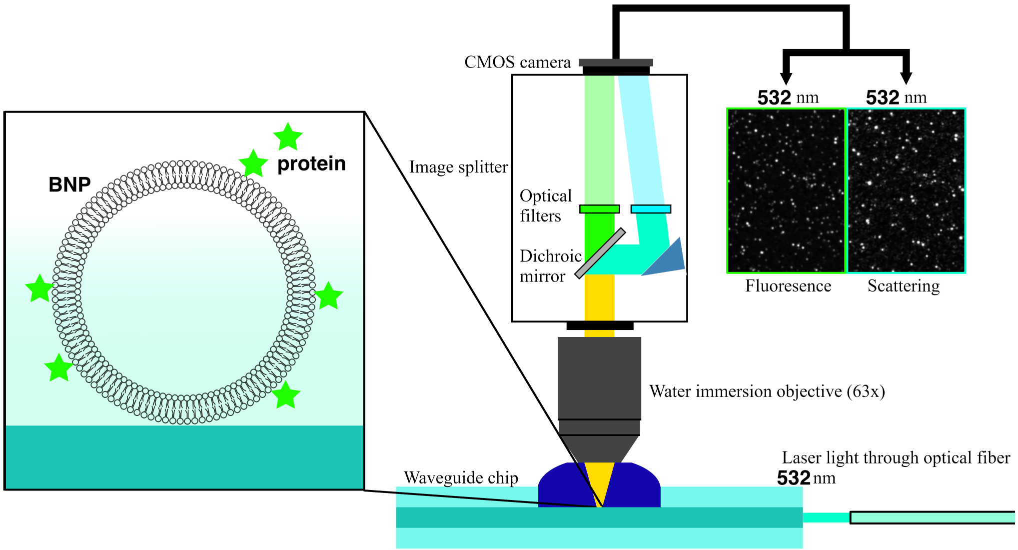

Figure 2.3: Schematic illustration of the microscopy setup, where the laser light illuminates a single BNP through the waveguide chip. Then the waveguide microscope monitors both the scattering and fluorescence signals of BNP that is present on the surface of the chip in a biological aqueous environment. Image is taken with permission from Sjöberg M. "Characterization of biological nanoparticles using evanescent field sensing.", Chalmers University of Technology; 2020[39].

2.2 Waveguide microscopy

Waveguide microscopy is a label-free surface-sensitive bioanalytical technique that uses an evanescent field to illuminate e.g. BNPs and generates both ensemble averaged and single-particle-resolved data [37]. Further, waveguide microscopy is capable of detecting both light scattering and fluorescence signals, which provides the possibility to observe both the labeled interior and exterior of the BNPs [37][29], Figure (2.3). Waveguide microscopy can be used in many various biotechnical applications such as characterization of an individual viruses, exosomes or in the investigation of the synthetic NPs that are used for drug or vaccine delivery[37][29]. Furthermore, waveguide microscopy can detect the so-called protein corona formation that has become a topic or interest in recent years in drug delivery development[37].

Due to the capability of single NP resolution of the waveguide microscopy, this technique can provide information about the distributions of properties of BNPs, such as composition, structure, and size [37] that, e.g., have a role in the cellular uptake[38]. Besides that, the waveguide can provide a real-time-monitoring of the scattering signal from single NPs and can simultaneously provide a fluorescence signal if the NP is fluorescence-labeled[38].

2.2.1 Fluorescence principle

As mentioned above, the waveguide microscopy can provide both a single-particle-resolved and an ensemble-averaging signal obtained from the fluorescence mode. Therefore, a short description of the basic principle of the fluorescence is presented here. The main principle of fluorescence can be described with the Jablonski diagram, shown in Figure (2.4). The diagram shows a fluorophore atom/molecule that is excited to a higher electronic states (S_i) from its ground state (S_0) upon absorbing the incident light, of wavelength λ_{in} [40].

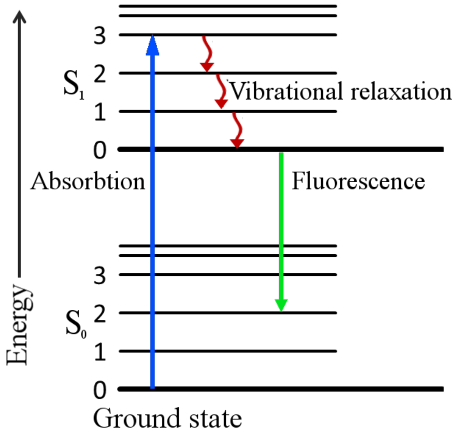

Figure 2.4: General Jablonski diagram illustrating the concept of fluorescence. The figure shows the processes of absorption, relaxation and both radiative (green arrow) as well as non-radiative emission (red arrows). Image is taken with permission from Sjöberg M. "Characterization of biological nanoparticles using evanescent field sensing.", Chalmers University of Technology; 2020[39].

At the S_i, the fluorophore molecule is not stable and is therefore deexcited back to its ground state through radiative and non-radiative pathways. The radiative process emits a photon, which corresponds to the energy gap between the S_i and S_0. This phenomenon is called fluorescence. The energy from the non-radiative process is mostly transferred to the environment. In a common absorption and emission spectrum, one can see that the absorption wavelength is a shorter wavelength than the emission wavelength. This can be explained by the Stokes shift [40].

It is worth mentioning that the fluorophore molecules besides that they can affect the structure of the BNPs upon binding to them, in which can effect the result [29][39], the fluorophore molecules can even undergo the so-called photo-bleaching fluorophore by continuously exposing it to light [41]. Therefore, in general the use of scattering modes has a number of advantages over using fluoresence modes but at the same it can give us a specific information of the sample of the interest and therefore fluoroscence mode instead can be used. Thus, waveguide microscopy is a adequate technique for the type of studies carried out in this thesis.

2.2.2 Waveguide chip

What makes waveguide microscopy unique is its chip, the single-mode waveguide chip, Figure (2.5). The waveguide chip has been developed by one of the thesis supervisors, Björn Agnarsson. It is consists of a silica layer with a refractive index of n_2=1.42. This silica layer is the core of the waveguide chip and it is sandwhiched between two symmetric layers of a material with a lower refractive index, the so-called CYTOP.

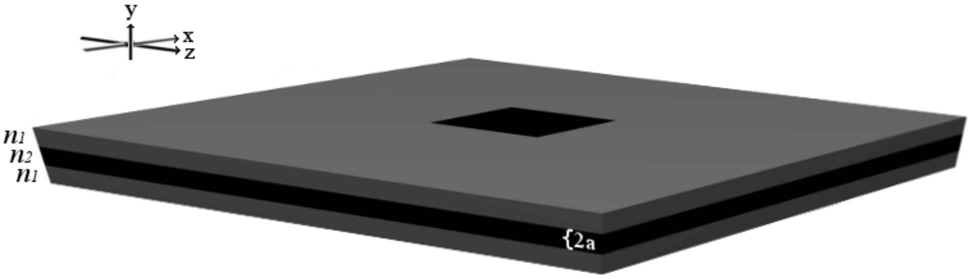

Figure 2.5: Each waveguide chip is 1x1 cm^2 big and in the middle of its upper face it has a 2x2 mm^2 well-etched hole that goes all way down to the waveguide core, where the sample is deposited on and illuminated by the evanescent field. Image is taken with permission from Sjöberg M. Characterization of biological nanoparticles using evanescent field sensing. Chalmers University of Technology; 2020[39].

CYTOP is an organic material that has a refractive index close to that of water, n_1=1.34 which makes it it ideal to reduce the stray light background during the measurements. A short description of the propagation of light in the waveguide chip is needed to better understand how a waveguide chip works. Describing light as a homogeneous wave and assuming the electric field to be an harmonic wave, the Helmholtz equation gives us

$$\nabla \mathbf{E} + k^2 n^2 \mathbf{E} = 0 \tag{2.3}$$

where $n = \sqrt{\epsilon_r}$ and $k = \omega/c$. From here, it is possible to approximate the propagation of light, in the core, as a plane wave in the x-direction, and assuming that z-direction is semi-infinite then we can express a trial solution in the form

$$\mathbf{E}(x, y) = \mathbf{E}(y)e^{-i\beta x} \tag{2.4}$$

where β is the wavenumber of light traveling in the waveguide in the x-direction. Putting together eq. 2.3 and 2.4 gives

$$\frac{\partial^2 \mathbf{E}}{\partial y^2} + (k^2 n_1^2 - \beta^2)\mathbf{E} = 0. \tag{2.5}$$

In our setup the incoupled light is generally linearly polarized and most often TE-linearly polarized, meaning that the electric field has only a component in the z-direction (E_z). We can thus postulate solutions that demonstrate the propagating electric field in the waveguide chip as

$$E_z = \begin{cases} A\cos(a\sqrt{k^2n_1^2-\beta^2}-\varphi)e^{-\sqrt{\beta^2-k^2n_1^2}(y-a)}, & y > a \\ A\cos(y\sqrt{k^2n_2^2-\beta^2}-\varphi), & -a < y < a \\ A\cos(a\sqrt{k^2n_1^2-\beta^2}+\varphi)e^{-\sqrt{\beta^2-k^2n_1^2}(y+a)}, & -a > y \end{cases} \tag{2.6}$$

where the refractive index of the core, n_2, is larger than the cladding layers n_1, a is the half-thickness of the core layer, A is a constant that can be derived from the boundary conditions of the propagating light, and φ is the phase term. From these equations, one can see that that the evanescent fields decay exponentially in the cladding layers, which enables to observe a BNP close to the surface.

The small thickness of the core layer allows only the fundamental mode to be sustained in the waveguide. What this means practically, is that as the light propagates through the waveguide core, an evanescent tail is formed at the boundary between the core and the cladding layers (CYTOP or water). This evanescent tail will have a characteristic penetration depth (d_p) that represents how far into the cladding environment its effect will be noticed. This penetration depth is defined from the the exponential term in equation (2.6), as the distance d_p at which point the field intensity has drooped to $1/e$ of the intensity at the cladding-core-layer interface ($y = a$). Or in other words:

$$d_p = \frac{1}{\sqrt{\beta^2 - k^2n_1^2}} \tag{2.7}$$

In general the propagation constant β will depend on both material properties (refractive indexes), geometrical properties (core layer thickness) and properties of the in-coupled light (wavelength and polarization). For a waveguide with a core-layer thickness of around 400 nm, n_1 =1.34, n_2=1.42, λ = 488, we get a propagation constant of 17,8 μm^{-1} which translates into penetration depth of around 228 nm. Hence, only objects within this penetration depth will interact with the propagating light and become visible in the microscope.

2.2.3 Scattering and fluorescence intensity by a small particle

In Rayleigh scattering theory, the phase of an incident electromagnetic wave interacting with a particle much smaller than its wavelength, is assumed to not be affected by the particle. Upon interaction the particle will experience an induced dipole moment $\mathbf{p}$ inside of itself according to

$$\mathbf{p} = \alpha\mathbf{E} \tag{2.8}$$

which defines the polarizability of the particle, α. The electric field of the scattered wave will be proportional to the dipole moment and the intensity thus proportional to the square of both the incident electric field and the polarizability. In general the scattering intensity can be represented as

$$I_s \approx A|\alpha|^2 \tag{2.9}$$

where A is function that includes the square of the evanescent field intensity.

If we assume that the model particle is a spherical shell (e.g. a model vesicle) with radius r, thickness of d with a refractive index of n_l; given that that both the inside and outside of this spherical shell has the same refractive index of n_m, the polarizability [39]

$$\alpha_v = \frac{4\pi r^2 d(2n_l^2 + n_m^2)(n_l^2 - n_m^2)}{3n^2 n_m^2} \propto r^2 \tag{2.10}$$

Furthermore, if the model particle has the same refractive index both inside as its shell, in another word said that the sphere is filled with the same material as its shell, then the polarizability will be([39])

$$\alpha_s = 4\pi r^3 \frac{n_l - n_m}{n_l + 2n_m} \propto r^3 \tag{2.11}$$

Inserting equation (2.10) or (2.11) into equation (2.9) gives us either the scattering intensity of a vesicle $I_{s,v}$ or a filled vesicle $I_{s,s}$

$$I_{s,v} = Af_s|\alpha_v|^2 \propto r^4 \tag{2.12}$$

or

$$I_{s,s} = Af_s|\alpha_s|^2 \propto r^6. \tag{2.13}$$

The readers interested in more details of the equations presented above, are referred to [39][29] and [42].

On the contrary, the intensity from the fluorophore molecules present in the particle of interest is proportional to the number of fluorophore molecules (N_f), leading us to fluorescence intensity for a vesicle ($I_{f,v}$) proportional to the vesicles area $A_{A,v}$,

$$I_{f,v} \propto N_f \propto A_{A,v} \propto r^2 \tag{2.14}$$

and fluorescence intensity for a filled-vesicle ($I_{f,s}$) proportional to the vesicles volume $V_{V,s}$,

$$I_{f,s} \propto N_f \propto V_{V,s} \propto r^3. \tag{2.15}$$

For further details of these equations, the reader is encouraged to read [29][39][42].

2.2.4 Waveguide microscopy setups and experimental

Waveguide setups. In Figure (2.3) we have already seen a schematic illustration of the whole waveguide microscopy setup, where laser light of 532 nm is coupled to the core of the waveguide chip through an optical fiber, where an exponentially decaying evanescent field is generated and illuminates the solution droplet on top of the chip, monitoring simultaneously the scattering and fluorescence signals of individual BNPs.

Waveguide chip. A closer image of the chip with the liquid droplet on top of it, is shown in Figure (2.6). In the droplet, a sequence of entities (PLL-g-PEG-biotin or SLB, SA, LNPs, then proteins) were added that bound to the previous entity either via electrostatically or via biotin-streptavidin interactions. Before adding each entity, the surface was rinsed a number of times with PBS in order to make sure that the previously liquid totally was removed. As shown in Figure (2.6), there is no pump machine coupled to the waveguide setup that can exchange the fluidity in the waveguide chip. Therefore we needed first to remove the current liquid and then replaced with the new one by pipetting. Changing the pH of the droplet was done in the same way.

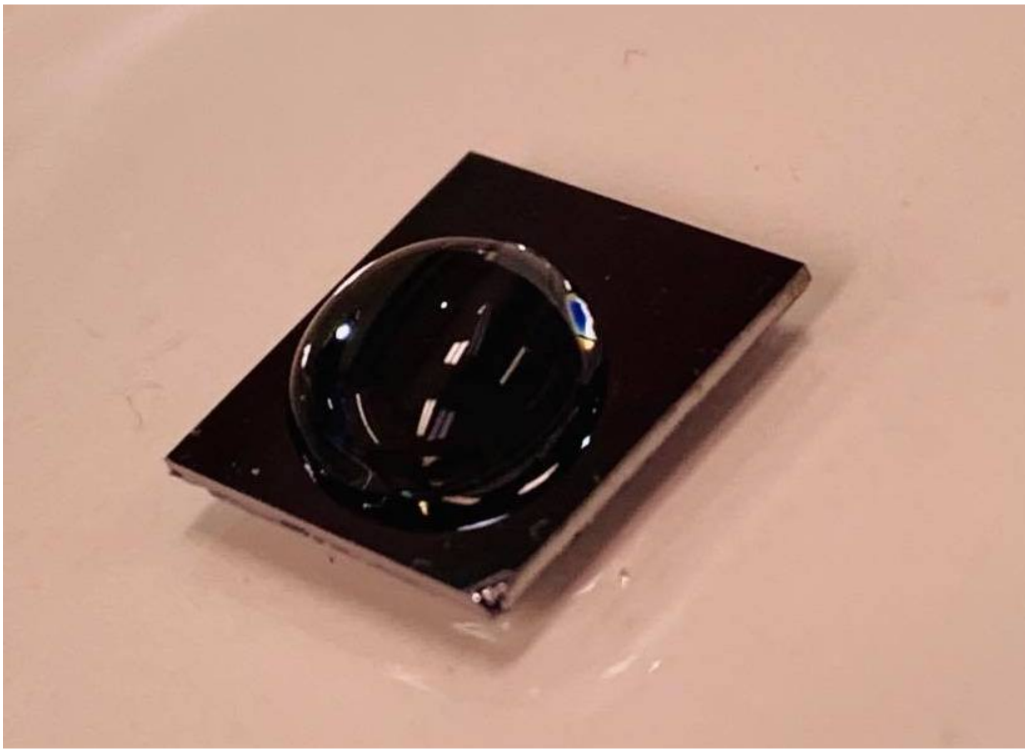

Figure 2.6: A liquid droplet of the sample on the waveguide chip.

Waveguide chip sensor surface cleaning. At the beginning of the work, prior to each experiment, the waveguide was rinsed with MilliQ water, followed by drying it with N2 gas and then placed into plasma cleaner machine in order to both destroy all the contaminations and activate the surface. During the experiments, we found out that a proper cleaning was needed since we could not obtain a proper functionalized surface.

Therefore, we started with a new cleaning protocol. First, the chip was rinsed SDS, MilliQ, and followed by drying with N2 gas. Further, the chip was placed into a plasma cleaner machine for ca. 15 minutes. Then a drop of sulfuric acid was placed on top of the chip for 15-30 minutes in order to remove all organic contaminations. Towards the end, the chip was rinsed again with MilliQ water and dried with N2 gas. With the new cleaning protocol, we were able to use the same chip during this thesis.

LNPs and ApoE concentrations used in the Waveguide microscopy. As mentioned above, waveguide microscopy can provide information based on a single individual NP close to the surface. Therefore it does not matter which concentration of LNP one uses in this technique. In that sense, waveguide microscopy measurements were of much low cost than the QCM-D ones. On the contrary, the concentration of ApoE was used during waveguide microscopy was 1-5 times higher than the concentration used in the QCM-D measurements.

2.3 Nanoparticle tracking analysis

Nanoparticle Tracking Analysis (NTA) have been used to both determine the concentration and the size distributions of the LNPs in this work. NTA is a technique capable of determining nanoparticle size and concentration both with scattering and fluorescent modes by tracking the particles' Brownian motion. NTA software analyzes many particles individually and simultaneously by using Stokes-Einstein equation (2.16) to determine the hydrodynamic diameter of the particle suspended in an aqueous environment.

$$\frac{\langle \bar{x}, \bar{y} \rangle^2}{4} = Dt = \frac{k_B T}{6\pi \eta r} \tag{2.16}$$

where $\langle \bar{x}, \bar{y} \rangle^2$ is the average distance each particle moves in x and y directions, T is at absolute temperature, k_B is Boltzmann's constant, D is diffusion constant, η is the solvent viscosity and finally r is the hydrodynamic radius [43]. The NTA instrument used in this thesis is a Nanosight LM10 with a Hamamatsu C11440-50B/A11893-02 camera and laser with a wavelength of 488 nm. The setup is equipped with a syringe pump to enable having a continuous flow rate during the measurements, especially when the instrument uses a fluorescent mode when the risk of photo-bleaching the studied particles is high, Figure(2.7).

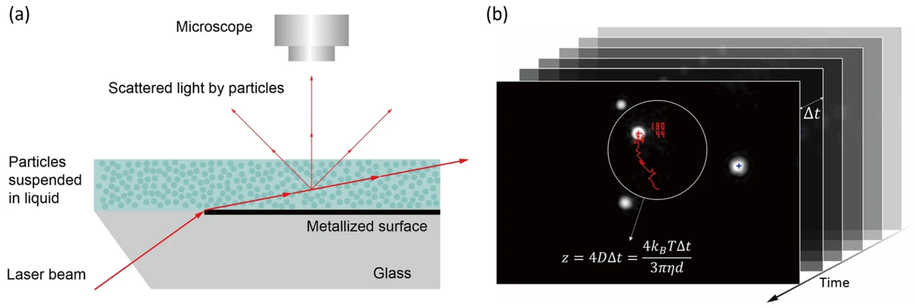

Figure 2.7: (a) Instrumental schematics of NTA detection, where the particles suspended in liquid and illuminated by laser beam. Light scattered by a the particles is detected, from which the position of the particles is identified by the software. (b) The software tracks the trajectory of the particles and constructs particle tracks. The image is taken with permission from Kim A, Ng WB, Bernt W, Cho NJ. Validation of Size Estimation of Nanoparti-cle Tracking Analysis on Polydisperse Macromolecule Assembly. Sci Rep. 2019Feb;9(2639):1–14[43].

2.4 Surface preparation

There are many ways to immobilize LNPs to the surface of a sensor. In this work, two different substrates have been used in order to functionalize the surface of the sensors, to which LNPs were bound via biotin-streptavidin interaction. The first surface (surface) was composed of co-polymer with a poly(L-lysine) backbone and poly(ethylene glycol) side-chains containing 5% biotin (PLL-g-PEG-5-%-PEG-biotin (PLL-g-PEG)) (purchased from Avanti). PLL-g-PEG is a hydrophilic and uncharged synthetic polymer that has a positively charged backbone (PLL-backbone), which is used to bind to a negatively charged substrate through an electrostatic interaction [44], Figure(2.8).

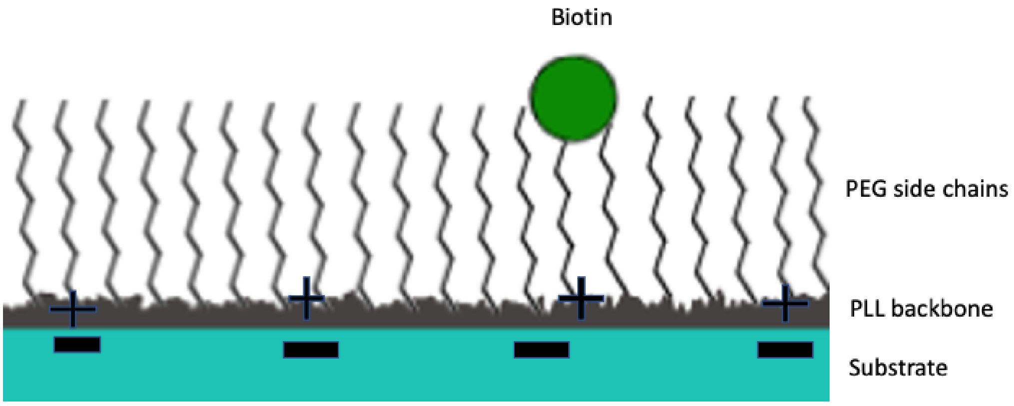

Figure 2.8: Surface chemistry1 composed of PLL-g-PEG-5-%-PEG-biotin. The image is adapted from with permission from Sjöberg M. "Characterization of biological nanoparticles using evanescent field sensing.", Chalmers University of Technology; 2020[39].

The second surface chemistry (surface2) that has been used was composed of supported lipid bilayers (SLB). An SLB is composed of phospholipids. A phospholipid consist of a hydrophilic head and two fatty acid tails that are hydrophobic, Figure (2.9). As shown in the image of the lipid, lipids used in this project usually have a length of 2.5 nm and a head-group of 0.5 nm^2, but not all the lipids have the same size as it can be seen in Figure (2.10), where the another type of lipid called CAP-biotin (green-circle) is slightly longer than the other ones. However, when lipids came into contact with the water molecules or a charged surface, the hydrophobic parts of the lipids hide themselves inside of the SLB and the head-group towards to the water molecules or to the activated surface sensor, Figure(2.10). In this work, the SLB was composed of 95-99%1-palmitoyl-2-oleoyl-glycero-3-phosphocholine (POPC) and 1-5% 1,2-Dipalmitoyl-sn-glycerol-3-Phosphoethanolamine-N-(CAP-biotin)(purchased from Avanti).

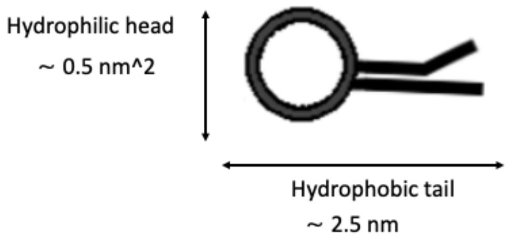

Figure 2.9: Illustration of a phospholipid. A lipid has usually 2.5 nm length and it has even an hydrophobic head of the size ca. 0.5 nm^2.

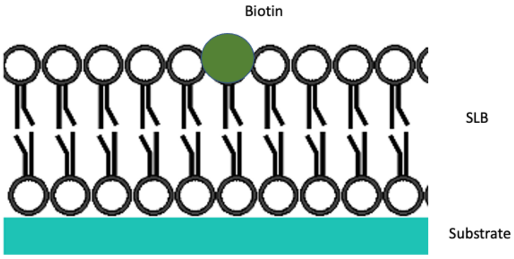

Figure 2.10: Surface chemistry2 (SLB) composed of POPC and CAP-biotin on a subtrate. The images are adapted with permission from Sjöberg M. "Characterization of biological nanoparticles using evanescent field sensing.", Chalmers University of Technology; 2020[39].

After the surfaces have been functionalized with a desired substrate through activating the surface with the plasma cleaner machine, LNPs were bound to them via biotin-streptavidin (from Sigma). Biotin and streptavidin are two proteins that are well known in the biophysics field. They bind to each other irreversibly due their high affinity (K_d) of about $K_d = 10^{-15}$ to 10^{-14} [45]. Furthermore, a each streptavidin (SA) can bind up to four biotines at the same time, shown in Figure (2.11).

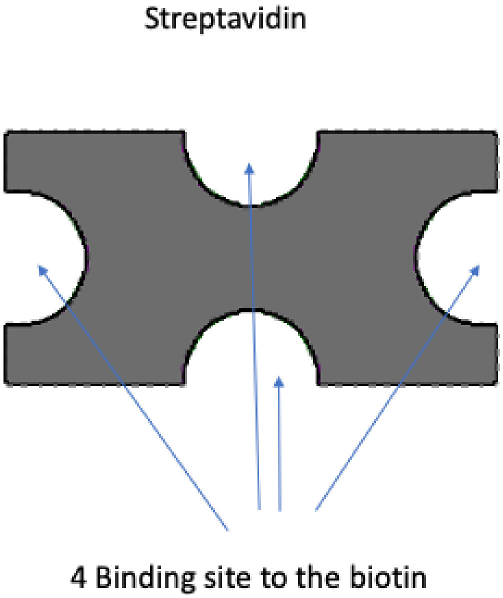

Figure 2.11: Illustration of a streptavidin with its four binding sites to biotin. Image is taken with permission from Sjöberg M. "Characterization of biological nanoparticles using evanescent field sensing.", Chalmers University of Technology; 2020[39].

2.4.1 Vesicle extrusion

In order to create SLBs on different sensor surfaces, lipid-bilayer vesicles containing 95-99%mol POPC and 1-5%mol CAP-biotin were created. Each lipid solution (POPC and CAP-biotin), originally dissolved in a chloroform solution, was mixed. In order to remove all the chloroform solution from the sample, the solution has been dried in a vacuum chamber for two hours. Then, PBS was added to the dried solution. When the lipids came into contact with the water, they enveloped themselves into spherical lipid-multi-layers due to the entropic reasons [46]. Furthermore, to obtain lipid-bilayers vesicles, the solution was froze-thrown five times [46]. Towards the end, to obtain a monodisperse vesicle solution, the solution was extruded 11 times through 100 nm poly-filters.

2.5 pH preparation

In order to vary the pH of the bulk solution that mimics the pH value of an endosome, different buffer solutions with different pH values were created following universal buffer protocol. The table below (2.1) illustrates the amount of citric acid ($C_6H_8O_7$) with a concentration of 0.1 M, disodium phosphate (Na_2HPO_4) with a concentration of 0.2 M, and sodium chloride (NaCl) with a concentration of 150 mM that was mixed to obtain a specific pH value for this work. All the material above was purchased from Avanti.

Table 2.1: pH preparation

pH	0.1 M $C_6H_8O_7$	0.2 M Na_2HPO_4	150 mM Nacl
7.4	-	-	-
6.6	5.45	14.55	200
6.0	7.37	12.63	200
5.6	8.40	11.60	200
4.6	10.65	9.35	200

For the pH 7.4, a tablet of the phosphate-buffered saline (PBS)(from Sigma) was directly dissolved into MilliQ water.

3

Results and discussions

The results and discussions of this thesis are all presented in three subsections. In the first subsection, the results and the discussions about which model surface chemistry is suitable for binding LNPs while being inert to varying pH is presented. Moreover, the size distributions of the LNPs obtained from the NTA are also presented. Once a suitable model surface chemistry was chosen, the results and discussions of corona formation on LNPs with different proteins (ApoE or a Apoe-BSA mixture) is introduced in the following subsections. Finally, in the last subsection, the effect of an adhered ApoE layer on LNPs upon a varying pH is presented, a phenomenon which is critical for the release of the cargo. Note that all the measurements were first performed with the QCM-D, and then, based on these results, continued with the waveguide microscopy.

3.1 Lipid nanoparticle binding to the surface

There are many different ways to immobilize LNPs on a sensor surface. In this project, two different model surface chemistries were studied by using QCM-D measurements at room temperature. The first surface chemistry chosen for this work consisted of PLL-g-PEG-biotin, see in section 2.4. The second model surface chemistry was a supported lipid bilayer containing POPC and CAP-biotin. The study of these model surface chemistries were first performed with the QCM-D and then continued with the waveguide microscopy. Further, size characterization of the LNPs was performed by NTA.

3.1.1 Surface chemistry 1 in QCM-D

In Figure (3.1), a cartoon of the first model surface chemistry chosen to bind LNPs on the QCM-D sensor surface is illustrated. The QCM-D sensor was functionalized with PLL-g-PEG-biotin, Figure (3.1, i). LNPs were then immobilized on the surface via SA, Figure (3.1 ii and iii). As illustrated in the graphs in Figures (3.2) and (3.3), the binding of each component (PLL-g-PEG-biotin, SA, and LNPs) to the surface results in frequency decreasing as well as the energy dissipation increasing. The solid lines show the binding of entities to the sensor's surface, while the dashed lines are the controls. The control measurement had been performed in order to see how the signals changes upon LNPs binding to the surface compared when there is no any LNPs.

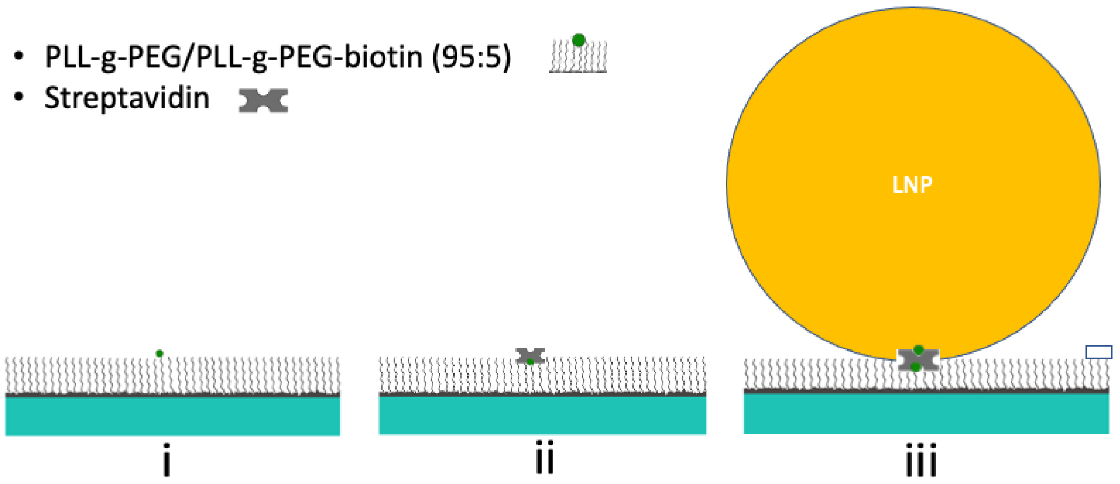

Figure 3.1: Schematic illustration of the binding of a LNP mimics (iii) to a fuctionalized surface with PLL-g-PEG-biotin (i) via streptavitin (ii).

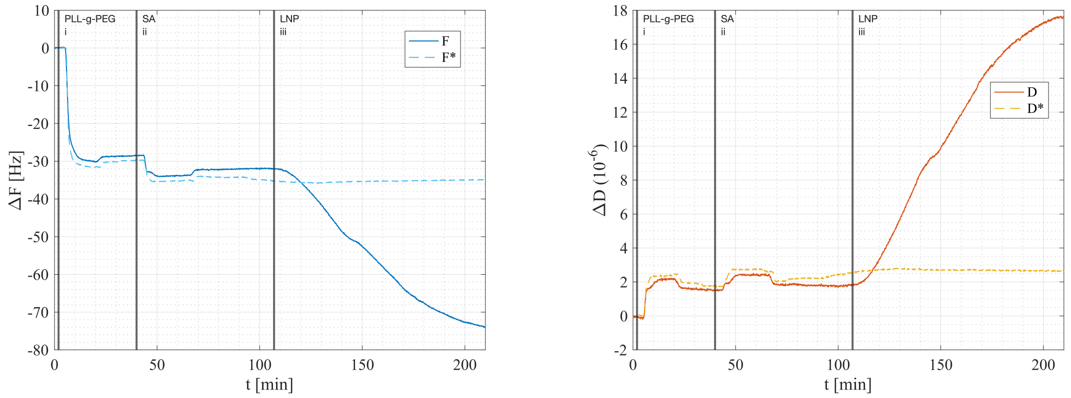

Figure 3.2: QCM-D measurement shows that the frequency decreases when each of the components: (i, ii and iii) bind to the model surface. The light blue dashed line is the control that results only from (i) and (ii).

Figure 3.3: QCM-D measurement shows that the energy dissipation increases when each of the components: (i, ii and iii) bind to the model surface. The light orange dashed line is the control that results only from (i) and (ii).

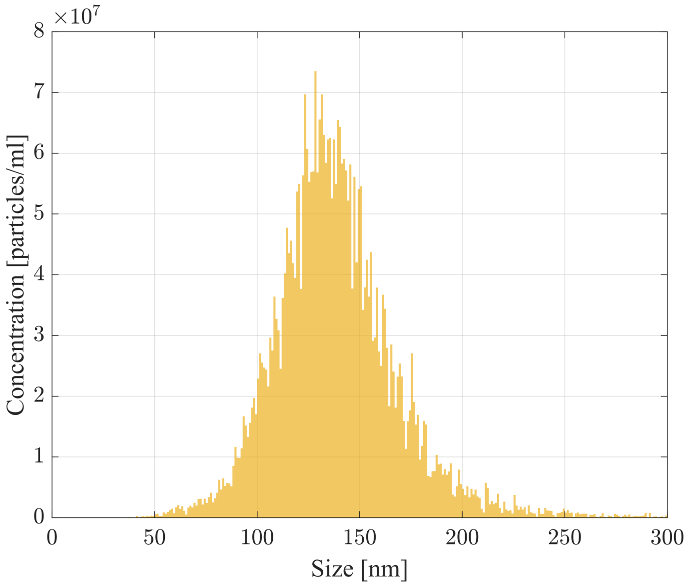

Figure 3.4: Size distribution of the LNPs in NTA. The mean size of the LNPs is ca. 138 [nm] with standard deviation of 14 [nm].

The frequency shift upon binding of each analyte to the sensor indicates a mass increase on the sensor through the Sauerbrey equation (2.2). The frequency graph shows that to obtain ca. a 30 Hz frequency response results from the binding of LNPs on the surface, when a volume of 0.45 mL and a concentration of $4\text{x}10^{10}$ mL^{-1} was used. This frequency response corresponds to ca. $2.7\text{x}10^{7}$ cm^{-2} LNPs on the surface. This assumes that an LNP has a spherical form with a hydrodynamic diameter of 138 nm as obtained from, Figure (3.4). Note that the QCM-D overestimates the bound mass due to the mass of the coupled water molecules[36].

3.1.2 Surface chemistry 2 in QCM-D

The second model surface chemistry candidate was used in this work consisted of the SLB. This SLB contained 95% POPC and 5% CAP-biotin, Figure(3.5,i). As in the previous subsection, the LNPs were conjugated to the surface via SA, Figure (3.5, ii and iii). Figures (3.6) and (3.7), show the frequency decrease and dissipation increase upon the adsorption of enteties to the sensor surface, as was expected. Figure (3.5) shows that the largest frequency shift results from binding of LNPs on the SLB, and it is estimated to be ca. a -205 Hz, which corresponds to $1.8\text{x}10^{8}$ cm^{-2} of LNPs on the sensor surface, using equation (2.2). The amount of LNPs used to obtain this frequency shift was less than half of the amount of the LNPs used in the first model surface chemistry.

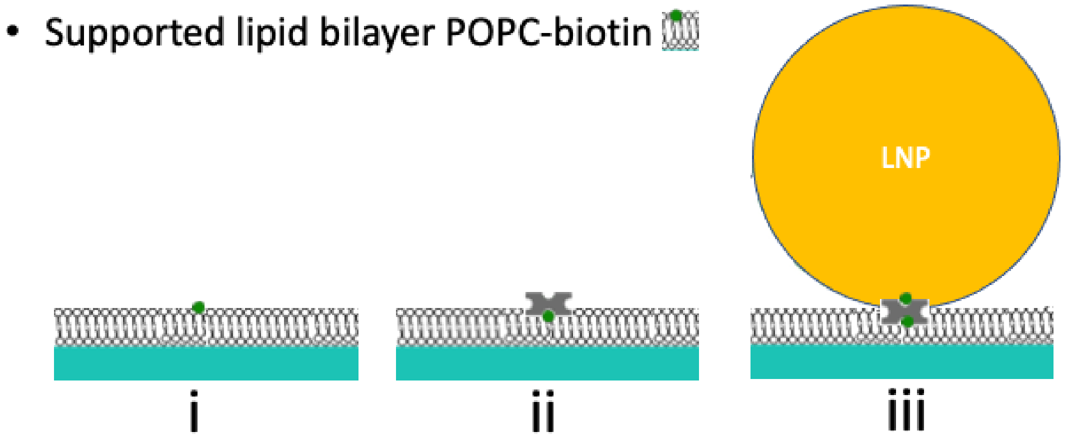

Figure 3.5: Schematic illustration of the binding of LNP mimics (iii) to a functionalized surface with PLL-g-PEG-Biotin (i) via streptavitin (ii).

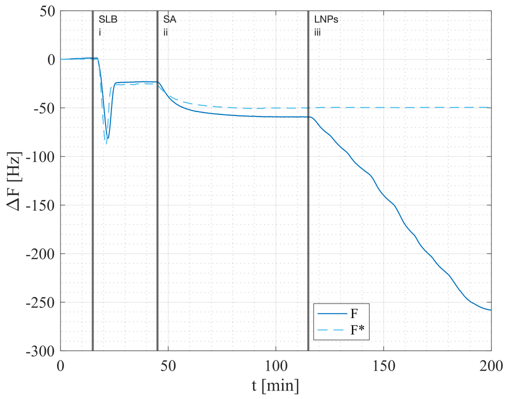

Figure 3.6: QCM-D measurement shows that the frequency decreases when each of the components: (i, ii and iii) binds to the model surface. The light blue dashed line is the control one that results only from (i) and (ii).

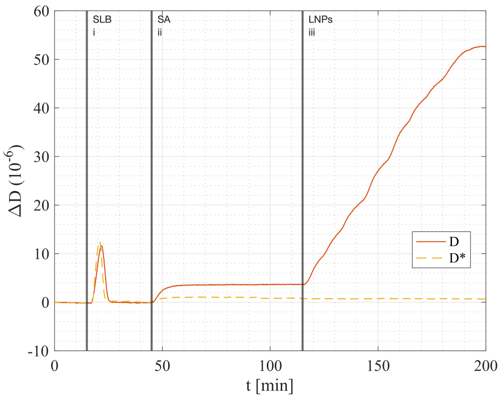

Figure 3.7: QCM-D measurement shows that the dissipation energy increases when each of the components: (i, ii and iii) binds to the model surface. The light orange dashed line is the control one that results only from (i) and (ii).

3.1.3 Control 1: Interaction of ApoE with surface 1 and 2 without any LNPs in QCM-D

In this section, we have studied the interaction between ApoE with the surface chemistries outlined above to observe if ApoE binds or not. The best candidate surface would be the one to which ApoE does not bind, or to which ApoE binds reversibly. Figure (3.8) shows the QCM-D responses when ApoE was added to the PLL-g-PEG-biotin functionalized surface. As a result, the frequency decreased and energy dissipation increased. This result might indicate that a small amount of ApoE had bound to the surface. There is also a small probability that these frequency and dissipation shifts upon adding ApoE, are due to the background noise. However, the frequency and dissipation response is very small upon ApoE injection to the surface.

Figure (3.9) show the results when ApoE was instead added to the SLB surface chemistry. The frequency decrease of 8 Hz upon adding ApoE suggests binding ApoE either to the SLB or the SA. As the system was rinsed and the pH was decreased to 6.6, the ApoE seemed to dissociate. In future work, one should study if this shift in frequency and dissipation results from ApoE binding to SLB or SA.

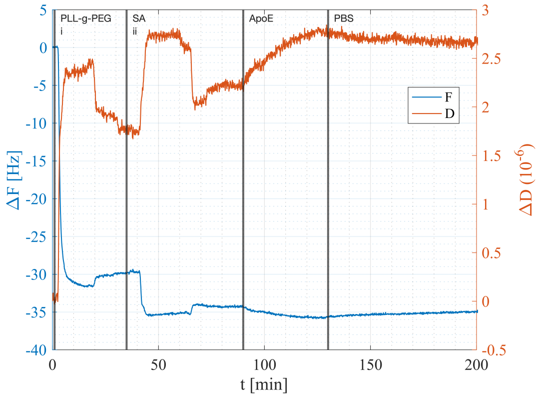

Figure 3.8: Interaction of ApoE with surface without any LNPs in QCM-D.

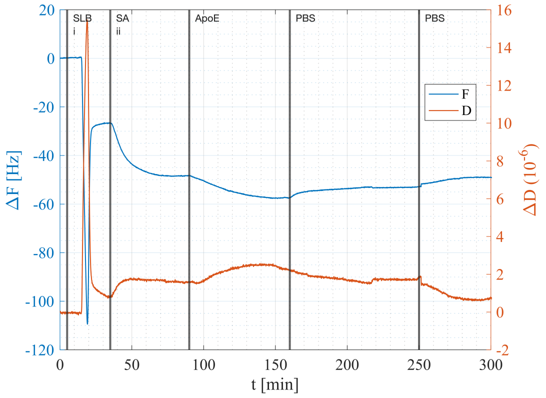

Figure 3.9: Interaction of ApoE with surface without any LNPs in QCM-D.

3.1.4 Control 2: Reaction of the surface 1 and 2 to the pH varying without any LNPs in QCM-D

This part aimed at finding which surface chemistry is inert to the varying pH. During the experiments, the pH was decreased step-wise from 7.4 to 6.6, 5.6, and 4.6 and then increased back to the initial pH of 7.4. Figures (3.10) and (3.11), both surfaces are compared to each other. The graph in Figure 3.10) shows when the surface was functionalized with the PLL-g-PEG-biotin. The result shows that the frequency response was increased, and dissipation was decreased upon pH lowering. This suggests that surface charges are affected and leading to partial dissociation of the objects from the surface. In contrast, the second model surface seemed to be stable at all pH, Figure (3.11).

The above results indicate that the SLB is the most suitable candidate as a substrate for our experiments, since LNPs bind easily to this surface. Further, the ApoE binds irreversibly to the SLB, as well the surface is being almost neutral for all pH values used in this work. Therefore, the study of the SLB was chosen for the waveguide microscopy measurements.

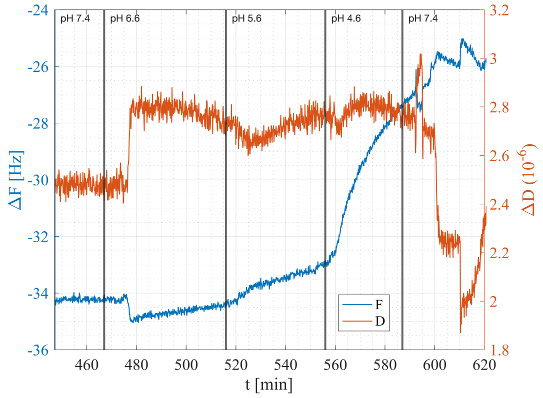

Figure 3.10: Reaction of the surface functionalized with the PLL-g-PEG-biotin to the pH varying without any LNPs in QCM-D.

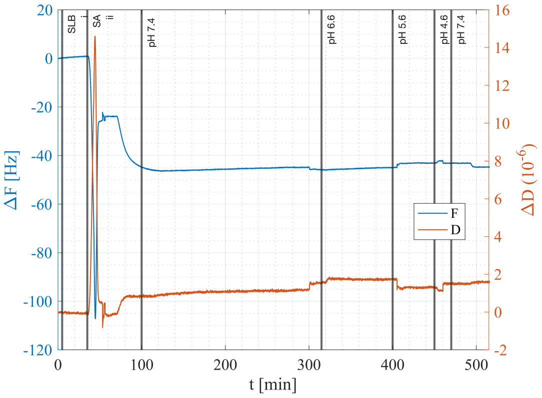

Figure 3.11: Reaction of the surface functionalized with the SLB to the pH varying without any LNPs in QCM-D.

3.1.5 Immobilization of the LNPs on SLB in Waveguide microscopy

Based on the information obtained from the QCM-D measurements, the immobilization of the LNPs to the SLB was studied with waveguide microscopy. Figure (3.12) shows an image of an SLB composed of 95% POPC and 5% CAP-biotin-lipids in scattering mode at wavelength 488 [nm]. As is illustrated in the image of the SLB on the waveguide microscopy chip, some islands of SLB (dark areas) seems to have formed among the adhered liposomes (bright spots). It was not possible to fully induce rupture of all adhered liposomes. This in-homogeneity in the SLB can be due to the high concentration of CAP-biotin-lipids, considering that POPC and CAP-biotin have a slightly different lengths and head group sizes. Moreover, the quality of the waveguide chip also had an effect on the homogeneity of the SLB as well as the way the chip was cleaned as it is described in the cleaning protocol of the waveguide chip, see section 2.2.4. Thus, the concentration of the CAP-biotin in the SLB was then reduced to 1% for the following waveguide microscopy.
.

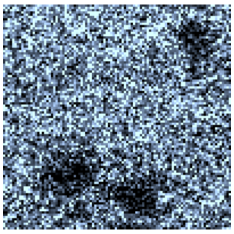

Figure 3.12: Un-homogeneous SLB on the waveguide microscopy chip taken at wavelength 488 [nm].

Figure (3.13) shows LNPs adhered through SA to the SLB composed of 99%mol POPC and 1%mol CAP-biotin. The images are taken with different wavelengths 635 and 532 nm. The first image to the left shows the cargo of the LNPs in fluorescence mode, while the middle one illustrates the RhD-DOPE lipids present in the LNPs. The last image illustrates the whole LNPs in scattering mode. Comparing these images with each other, it is clear that all LNPs had cargo. Note that these images are zoomed in on the whole surface, and we can see more particles in the whole image.

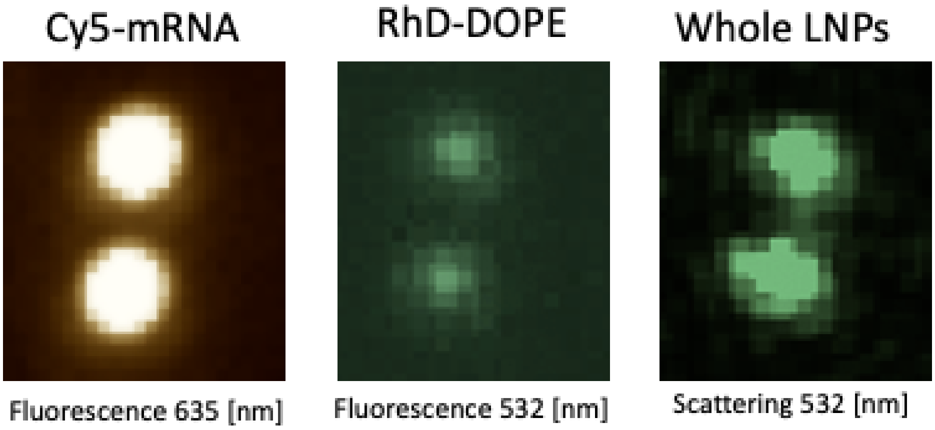

Figure 3.13: Images of the LNPs on the SLB via SA on waveguide chip. The Figure to the left shows the fluorescence image of the cargo exited with wavelength 635 [nm]. The middle Figure illustrates the fluorescence image of the RhD-DOPE lipids in the LNPs exited at 532 [nm]. The last Figure shows the whole LNPs image, which results from the scattering mode of the waveguide microscopy.

It is also worth mentioning that from this Figure (3.13), it is possible to analyze the size distribution of the LNPs and then compare with the NTA s, but this is not taken into account in this master thesis. From this result, it is clear that waveguide microscopy can provide information both from the interior and exterior of a single LNPs. Besides that, it in principle only needs a single LNP to obtain data using this instrument, which makes the experiments much more low-cost compared to the QCM-D.

3.2 Protein corona formation

As mentioned in the introduction, one of the most critical steps for the LNPs to be taken up by a targeted cell is that they are covered by the so-called, protein corona which mainly consists of serum proteins like e.g. ApoE, after LNPs have been exposed to a biological fluid. ApoE can only be absorbed on the surface of the LNPs after PEG-lipids have left the LNPs in the process called PEG-shedding. In line with this, in this section we present results from QCM-D and waveguide microscopy measurements when studying corona formation on the LNPs with different proteins. Here, all bound LNPs on the SLB were rinsed either with PBS or PBS and BSA for 60-90 minutes in order to induce PEG-shedding.

3.2.1 Protein corona formation in QCM-D

Figures (3.14) shows corona formation on the LNPs with ApoE in the QCM-D measurement. The bound LNPs to the SLB via SA were rinsed only with PBS. Afterward, ApoE was added to the surface with a continuous flow. Shifts in frequency and dissipation indicate that ApoE binds to the LNPs. The result shows a -55 Hz frequency response upon ApoE binding compared to the -205 Hz from the previously bound LNPs LNPs (thus a ratio of approximately 0.26). Further, the dissipation signal increasing indicates that the soft of the LNPs is increased upon ApoE binding.

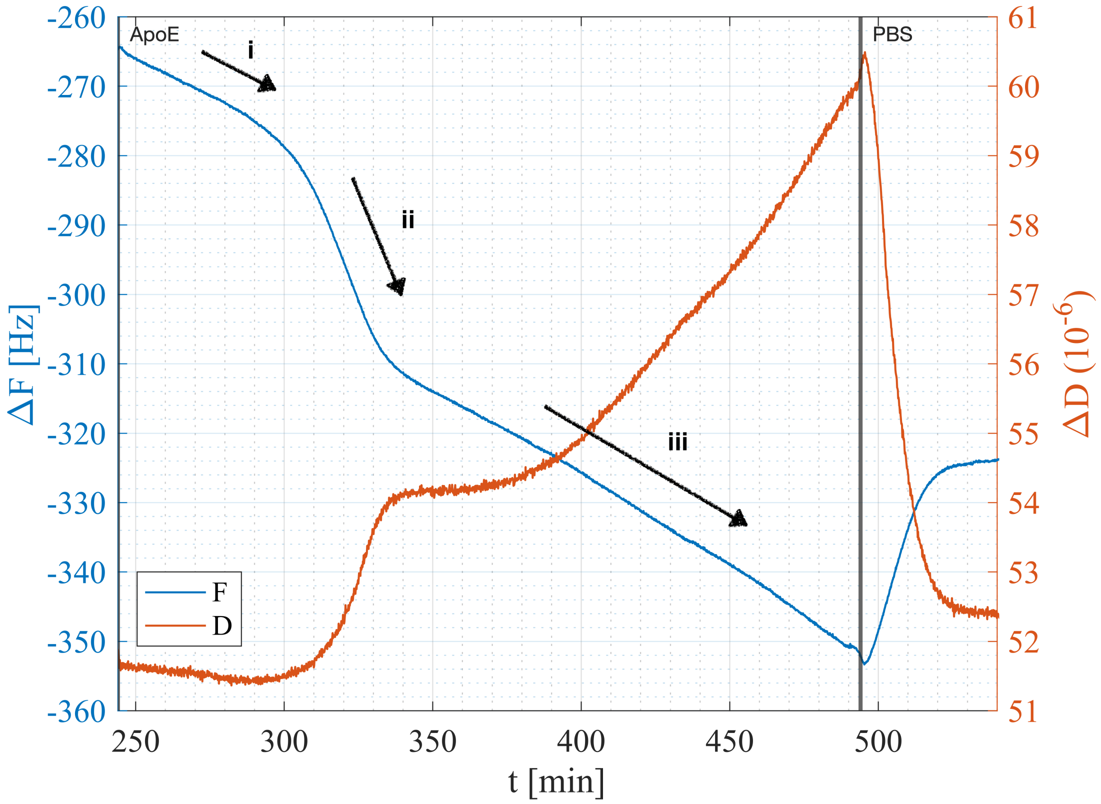

Figure 3.14: ApoE binding to the previously bound LNPs on SLB via SA in QCM-D. ApoE binds with three different phases shown by the black arrows: i, ii and iii. The solid blue line shows that the mass increases on the sensor surface as well dissipation increases (solid orange) upon adding ApoE.

As can be seen in these curves, ApoE binds to the LNPs with three different kinetic phases (i, ii, and iii). The first kinetic phase (3.14, i), appears to be slower than the two remaining phases, Figure (3.14, ii and iii). This possibly indicates that PEG-shedding was occurring, causing the ApoE binding to the LNPs to be slow. In the subsequent phase, ApoE binding seems to occur quickly, Figure (3.14, ii), suggesting that ApoE binds well to LNPs after some amount of the PEG-lipids have been washed away by the buffer. In the third part of the ApoE kinetic phase, it can be seen that the ApoE interaction with the LNPs is slowed down compared with the second kinetic phase. This might indicate that the ApoE binding starts to saturate. It might also be the case that LNP surfaces are saturated with ApoE but further binding is due to ApoE-ApoE interactions.

When the system was rinsed with PBS around time 500 min, it could be seen that the frequency started to increase and the dissipation response decreased, Figure(3.14). The energy dissipation response upon rinsing with PBS was much larger than for the frequency, suggesting that ApoE-ApoE interaction might have caused some kind of aggregation on the LNPs. In addition to this speculation, this result might suggest that almost all ApoE bound during the final binding phase (iii) is rinsed away by the buffer observing that energy dissipation returns to the same level as binding phases (i) and (iii).

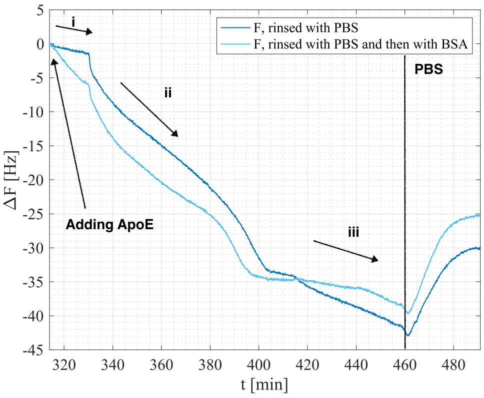

Figure 3.15: ΔF upon ApoE binding to the previously bound LNPs, normalized to the absolute response at t = 315 min giving ΔF(t=315 min)=-170 Hz. The light-blue curve results from when the LNPs were rinsed with PBS and the with BSA. The dark-curve comes from when the LNPs were rinsed with only PBS.

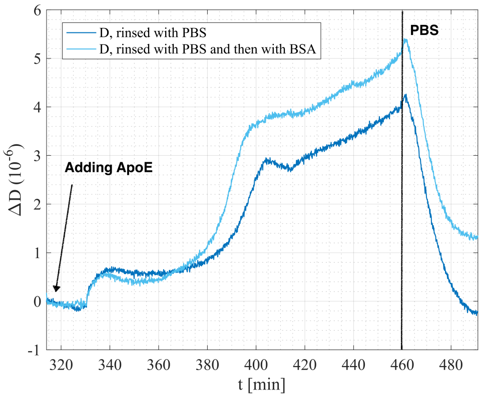

Figure 3.16: ΔD upon ApoE binding to the previously bound LNPs, normalized to the absolute response at t = 315 min giving ΔD(t=315 min)= 32(10^{-6}). The light-blue curve results from when the LNPs were rinsed with PBS and the with BSA. The dark-curve comes from when the LNPs were rinsed with only PBS.

In addition, the almost similar kinetic phases of ApoE binding to the LNPs have been observed when the system has been rinsed with the BSA, Figures (3.15) and (3.16). However, an important difference between the two measurements was observed, that the BSA seemingly that removed PEG-lipids and promoted earlier ApoE binding, Figure (3.15) and (3.16). The light-blue lines show the result from ApoE binding to the LNPs after the surface has been rinsed with the PBS and then with BSA and the light-blue lines result from when the system was rinsed with only PBS.

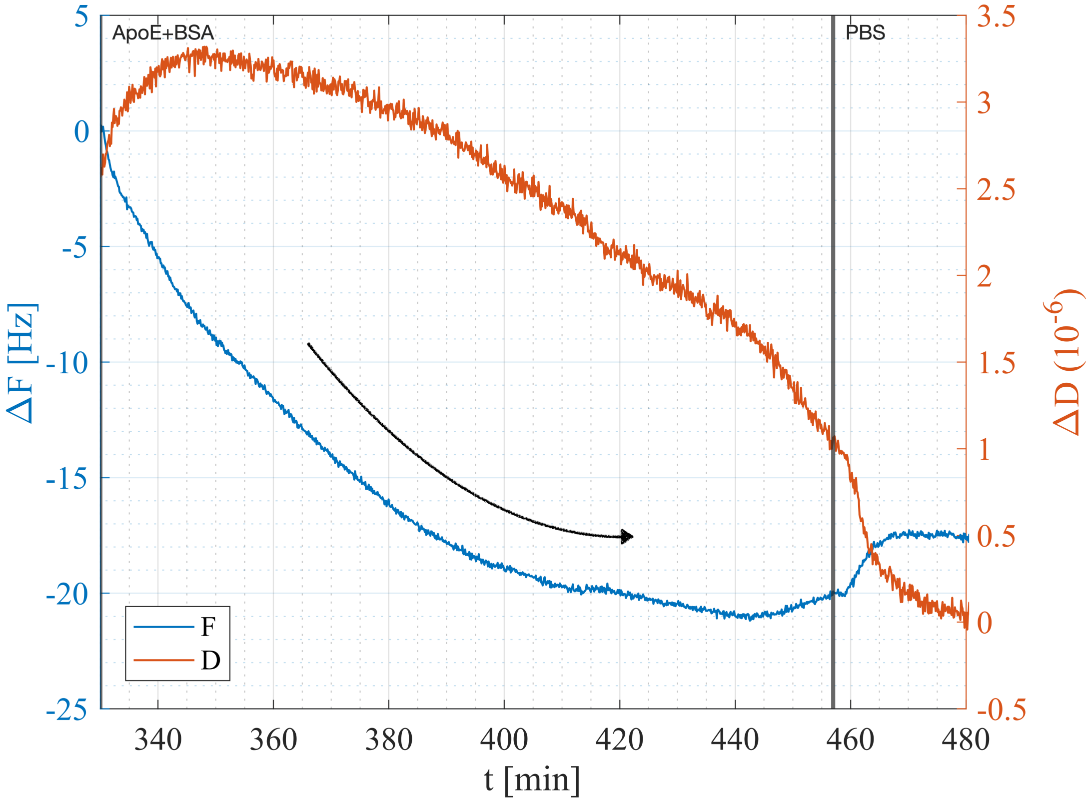

Figure 3.17: ApoE and BSA binding to the previoulsy bound LNPs on the SLB via SA in QCM-D. ΔF and ΔD are normalized to the absolute response at t= 330 min giving ΔF(t=330 min)=-160 Hz and ΔD(t=330 min)=30(10^{-6}).

Contrary to the kinetic phase from only ApoE binding to the LNPs, Figure (3.17) shows that the binding of a mixture of ApoE-BSA occurs monotonically before flattening out. Prior to the experiment, the bound LNPs were rinsed with PBS. A frequency response of 17 Hz was observed upon ApoE binding to the LNPs (which themselves produced a response of 93 Hz upon binding to the sensor surface), giving a ratio between ApoE and LNPs ca. 0.18. As can be seen in the result, at the beginning of the measurement, the dissipation response increased afterwhich it decreased upon ApoE binding, while the frequency response continued to decrease. These curves indicate that the ApoE might be bound more compact to the LNPs. Therefore, the dissipation response curve is not soft, as shown in Figure (3.14). Towards the end, the frequency did not increase as much as in Figure (3.17).

3.2.2 Protein corona formation in waveguide microscopy

In order to gain further understanding of the system investigated with QCM-D in Figure (3.14), it was additionally studied using waveguide microscopy. The LNPs were bound to an SLB via SA. Since the current waveguide microscopy setup do not yet provide the possibility of measuring under continuous flow, the surface was rinsed with PBS by pipetting a couple of times. ApoE was then added to the surface. The result of the experiment is shown in Figure (3.18). As can be seen in the result, the intensity did not increased upon adding ApoE, which suggests that there have been not interaction between ApoE and LNPs.

However, we were not able to observe binding between ApoE and LNPs as we could see in QCM-D measurements, although different concentrations of ApoE were tested. This indicates that PEG-shedding needs to occur for ApoE binding to happen. For PEG-shedding to occur, the bound LNPs need to be rinsed with buffer with a continuous flow, which was not possible to be performed with the current waveguide microscopy setup. Thus, future work should therefore include further developments of the waveguide microfluidic chip in order be able to rinse the surface with a continuous flow to promote PEG-shedding.

Also note that it is still possible that ApoE binding did occur, but did not produce a signal detectable due to the signal being small to be detected. This observation is supported by the QCM-D measurements that ApoE response is much smaller than the LNPs', even though a lot of materials were used to obtain an average signal in the QCM-D.

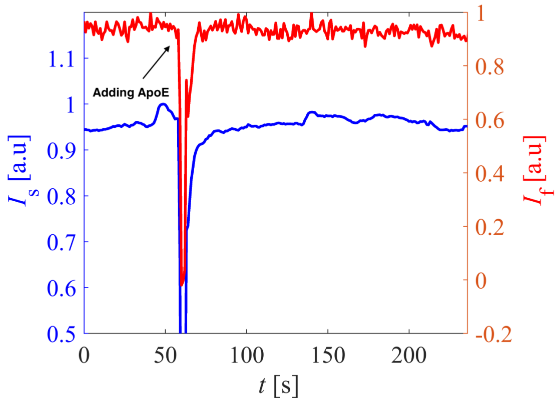

Figure 3.18: Scattering and fluorescence average intensity of all the LNPs over time upon adding ApoE in waveguide microscopy at wavelength 488 nm. The drop in intensity results from when the solution droplet was mixed by pipetting which lead to a temporary loss of intensity.

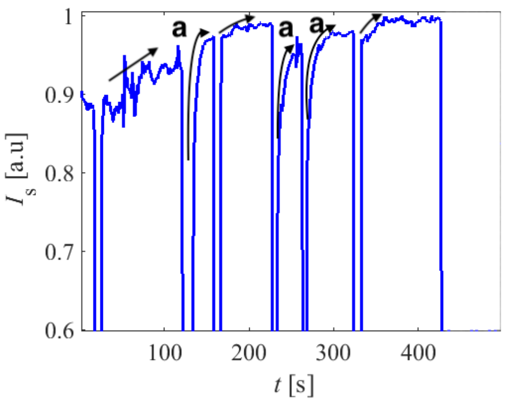

Figure 3.19: Scattering average intensity of all the LNPs over time upon adding ApoE to the surface in waveguide microscopy at wavelength 488 nm. The drops in intensity results from when the solution droplet was mixed by pipetting which lead to a temporary loss of intensity.

Since we could not see any binding of ApoE to LNPs in the waveguide microscopy as in the QCM-D measurement, the experiments was continued with a few modifications. To promote PEG-shedding, the LNPs were diluted and kept in the fridge for two days. Moreover, before the measurement, the temperature of the LNPs temperature increased to the body's temperature to potentially promote PEG-shedding. Then, the LNPs were bound to an SLB via SA and rinsed many times with PBS by pipetting. In the final stage, ApoE was added to the system.

The result of the experiment is shown in Figure (3.19). It shows that the average scattering intensity of all particles, after time 500s, started to increase. After that, the LNPs were exposed to a five times higher concentration of ApoE used in the QCM-D measurement. This type of intensity increase was not observed in the previous waveguide microscopy measurements. The drops in intensity in the curves results from when the solution droplet was mixed by pipetting which lead to a temporary loss of intensity. This result suggests that ApoE binding to LNPs might have occurred, especially in points "a" are typical characteristics for protein binding to the particles in the waveguide microscopy is seen, but we can not claim that we have seen ApoE binding to the LNPs. Further investigations are needed to confirm this observation.

3.3 Effect of a decreasing pH on bare and protein covered lipid nanoparticles

As mentioned in the introduction, LNPs covered by a layer of proteins are expected to undergo structural changes in the acidic internal environment of the endosome during the process of cargo release to the cytosol. Thus, here we present the results from QCM-D and waveguide microscopy measurements when lowering the pH of the environment surrounding bound LNPs both bare or pre-exposed to a protein solution (ApoE and BSA). The exposure to a protein solution models the LNP interaction with serum which occurs prior to cellular uptake in vivo.

3.3.1 Lowering pH for LNPs pre-exposed to protein solutions in QCM-D

Figures (3.20) and (3.21) present the results from QCM-D measurements when the pH were lowered gradually for the LNPs pre-exposed to different proteins. The blue colors show when the bound LNPs were only rinsed with PBS and BSA and followed by exposure to ApoE, yielding results similar to those shown in Figure (3.14). The purple curves show when the bound LNPs were rinsed with PBS and exposed of the mixture to a protein solution containing ApoE and BSA, i.e. the same measurement as shown in Figure (3.17).

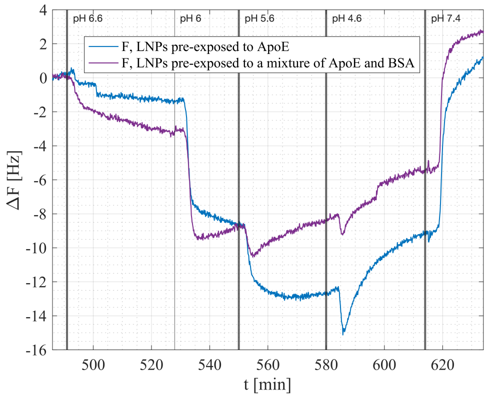

Figure 3.20: ΔF response upon pH decrease of the LNPs pre-exposed to the ApoE (the blue curve) and to mixture of the ApoE-BSA (purple curve) in QCM-D. ΔF is normalized to the absolute response at t= 488 min giving ΔF(t=488 min)=-185 Hz.

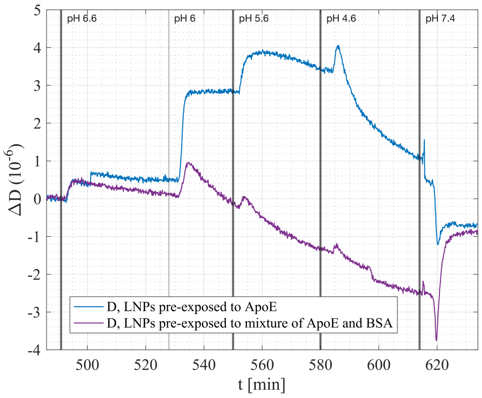

Figure 3.21: ΔD response upon pH decrease of the LNPs pre-exposed to the ApoE (the blue curve) and to mixture of the ApoE-BSA (purple curve) in QCM-D. ΔD is normalized to the absolute response at t= 488 min giving ΔD(t=488 min)=32(10^{-6}).

As is illustrated in the graphs, by lowering pH value, both the mass and the dissipation increases. These results possibly suggest structural changes in the LNPs. One explanation can be that the LNPs might have deformed and expanded their surface area thus allowing for more water molecules to bind to them, resulting in an increase in mass on the QCM-D sensor chip. Moreover, another explanation can be that more water molecules have entered inside the LNPs. Comparing the two graphs shown here, the blue and the purple one, the frequency response of the blue curve (LNPs pre-exposed to the ApoE) decreased, and the dissipation response increased until pH value 4.6. On the contrary, when a mixture of ApoE-BSA covered LNPs, the frequency response increased only until pH value 6.0, and the dissipation response increased only at the beginning of the pH 6.0, and then it continues to decreases.

This result indicates that comparing these proteins solutions (ApoE and ApoE-BSA), the mixture of ApoE-BSA acts more as a shelter for the LNPs and makes them less sensitive to a varying pH in the environment compared to when the LNPs were only pre-exposed to ApoE. However, in both cases, it can be seen that most structural changes in the LNPs have occurred at pH 6.0, which was expected since the MC3 has a pKa pH value at 6.44. In future work, more pH steps around this pH 6 could be added in order to find exactly at which pH the LNPs react.

Another similarity between these results is observed to occur around pH 4.6. In both cases, the frequency and dissipation response show similar behaviors at this pH value. These results suggest that some entities are leaving the surface, which could potentially be related desorption of some ApoE. Since ApoE has a pKa at 5.65, and will thus become positively charged at a pH below this, it might leave the LNPs, which in turn the LNPs are also positively charged. Further, toward the end, when the pH is increased back to pH 7.4, the frequency and dissipation responses have returned almost to the same value as before the pH decrease.

3.3.2 Comparison between stepwise and instant pH decrease in QCM-D

In this section, we compared the pH value lowered directly to 4.6 with when the pH value was lowered stepwise on the previously bound LNPs that have been pre-exposed to ApoE in the QCM-D instrument. The results from the experiments are of shown in Figures (3.22) and (3.23). The pink curves shows when the pH was decreased directly to 4.6 from 7.4 and back again to the initial value of 7.4. The blue curves, which is the same curve as illustrated above Figures (3.20) and (3.21), show when the pH was lowered stepwise from 7.6 to 6.6, 6.0, 5.6, 4.6 and again back to the initial value of 7.4. As can be seen in these results, the total frequency and dissipation shift upon increasing the pH is almost the same. Furthermore, in both cases, ApoE desorption occurs at pH 4.6 and has similar desorption kinetics.

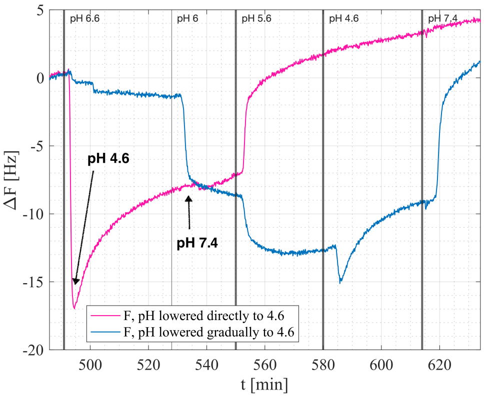

Figure 3.22: ΔF response upon pH decrease of the LNPs pre-exposed to the ApoE. In the pink curve, the pH is lowered directly. Meanwhile in the blue curve, the pH is lowered stepwise. ΔF is normalized to the absolute response at *t*= 488 min giving ΔF(*t*=488 min)=-187 Hz.

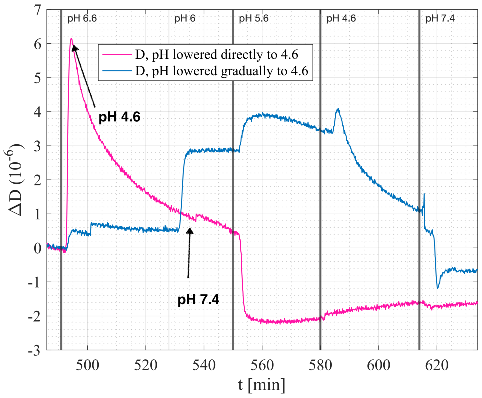

Figure 3.23: ΔD response upon pH decrease of the LNPs pre-exposed to the ApoE. In the pink curve, the pH is lowered directly. Meanwhile in the blue curve, the pH is lowered stepwise. ΔD is normalized to the absolute response at *t*= 488 min giving ΔD(*t*=488 min)=33(10^{-6}).

3.3.3 Comparison between bare and protein covered LNPs upon pH changes in QCM-D

In this part, we aimed to observe if there were any differences in structural changes for LNPs with and without preexposure to the ApoE when the pH value was lowered stepwise from 7.6 to, 6.6, 6.0, 5.6, 4.6 and then back to the initial pH value of 7.4. Prior to the experiments, the LNPs were bound to an SLB via SA and the rinsed with PBS. Figures (3.24),(3.26),(3.25) and (3.27) show the results of experiments that was carried out in QCM-D instrument. Graphs in Figures (3.24) and (3.26) result from when the LNPs were pre-exposed to ApoE, while the graphs in Figures (3.25) and (3.27) came from bound LNPs were not pre-exposed to ApoE. In the case of LNPs covered with ApoE, they reacted to the pH 6.6 faster compared to the when the LNPs without presxposed to ApoE. In addition, at pH 5.6, we can see the same phase kinetic of structural changes in both cases, which was expected since the MC3 that are present in the LNPs starts to protonate at pH 6.44.

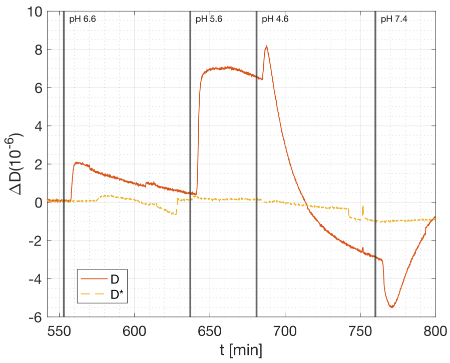

Figure 3.24: ΔD shifts upon pH decreases of the LNPs with ApoE. The dashed line is the control. ΔD is normalized to the absolute response at t= 540 min giving ΔD(t=540 min)=52(10^{-6}).

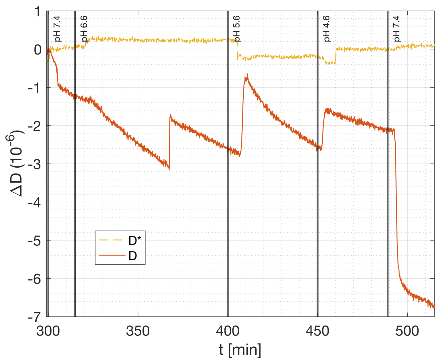

Figure 3.25: ΔD shifts upon pH decreases of the LNPs without ApoE. The dashed line is the control. ΔD is normalized to the absolute response at t=300 min giving ΔD(t=300 min)= 45(10^{-6}).

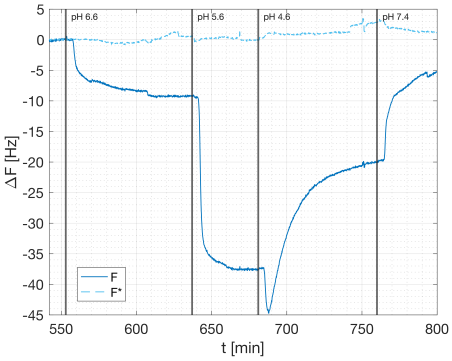

Figure 3.26: ΔF shifts upon pH decreases of the LNPs with ApoE. The dashed line is the control.ΔF is normalized to the absolute response at t= 540 min giving ΔF(t=540 min)=-320 Hz.

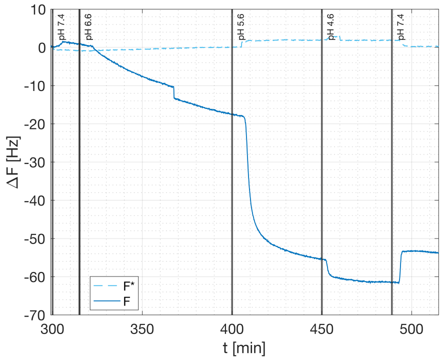

Figure 3.27: ΔF shifts upon pH decreases of the LNPs without ApoE. The dashed line is the control. ΔF is normalized to the absolute response at t= 300 min giving ΔF(t=300 min)=-215 Hz.

Another difference between these results can be seen at pH 4.6 in Figures (3.24) and (3.26), where both the mass and dissipation response are decreased where the ApoE covered the LNPs. These results possibly indicate that some ApoE dissociation has occurred. Meanwhile at Figures (3.25) and (3.27), the LNPs without ApoE still were undergoing a structural changes at pH 4.6. Furthermore, these curves suggest that the structure of LNPs have changed differently, depending on if they have been preexposed to the ApoE or not. However, there is a need to study this process further to understand why LNPs preexposed to ApoE are more sensible to 6.6 pH.

3.3.4 Comparison between bare and protein covered LNPs upon pH changes in waveguide microscopy

Based on the QCM-D measurements that LNPs without ApoE showed a slightly more significant structural change upon lowering the pH. In this part, we aimed to study if it is possible to see any differences in the structural changes when the LNPs are preexposed to the ApoE and when they are not using waveguide microscopy. Figure (3.28) shows a scatter plot of the bound LNPs without any preexposure to ApoE at pH 7.4 and pH 4.6. Before the experiments, the LNPs were bound to an SLB via SA and the rinsed with PBS by pipetting and afterwhich the pH was decreased to 4.6. As is seen in the result, the intensity of the LNPs decreased when the pH was lowered to 4.6. The intensity decrease is also apparent in the histograms shown on the scatter plots axes, which indicate that the population intensity is shifted down.

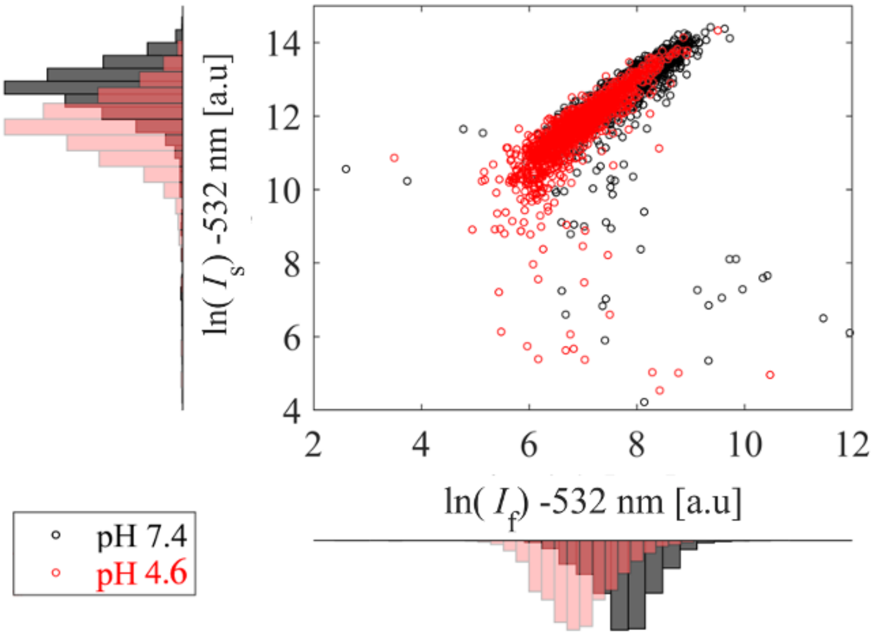

Figure 3.28: Scatter plots from the log-log plot of the scattering signal (whole LNPs) versus the fluorescence signal (from RhD-DOPE) of the bound LNPs not preexposure to ApoE at pH 7.4 (black histogram and circles) and pH 4.6 (red histogram and circles), at wavelength 532 nm.

Moreover, during the experiment, when the pH was decreased directly down to 4.6, the LNPs became more mobile, and suddenly the LNPs became blurred and smaller. Figures (3.29) and (3.30) illustrate both images and signals obtained from scattering and fluorescence mode of a single LNP during the pH decrease at wavelength 532 nm. These graphs and images of the LNP possibly indicate that either LNP has gone further away or got closer to the SLB, perhaps causing fusion. The second option is more likely to occur since the POPC in the SLB is slightly negatively charged.

Thus, by decreasing pH in bulk, the MC3 present in the LNPs are protonated, leading to an interaction between LNPs and the SLB. Unfortunately, a quantitative theory to account for how much an LNP is fused with the SLB has not yet been formulated. Thus, in future experiments, one should consider varying the amount of the RhD-DOPE-lipids on the LNPs to observe how much and how fast the fusion of the LNP occurs with the SLB.

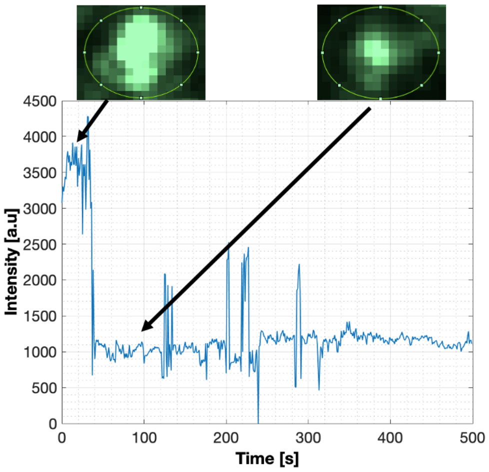

Figure 3.29: Scattering intensity of a single LNP over time when the pH was lowered to 4.6.

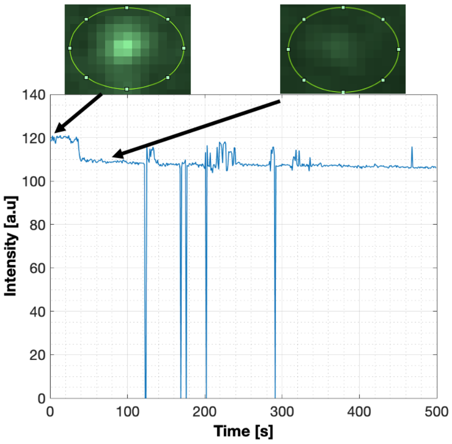

Figure 3.30: Fluorescent intensity of the same LNP over time upon pH decreasing to 4.6.

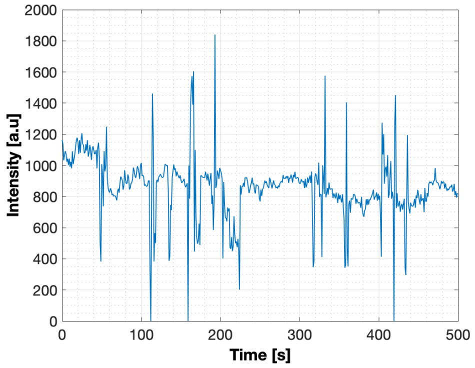

Figure 3.31: Scattering intensity of the same LNP over time when the pH was increased back to the initial pH of 7.4.

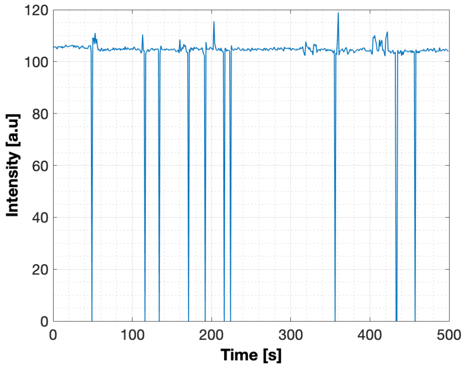

Figure 3.32: Fluorescent intensity of a single LNP over time when the pH was increased back to the initial pH of 7.4.

Figures (3.31) and (3.32) illustrate both the scattering and fluorescence signals when the pH was increased back to the initial value of 7.4 from pH 4.6. As illustrated in the graphs, the signal did not return to the initial value upon the increase of pH.

In figure (3.33) we show images of different parts of LNPs at three stages in a process where the environment changes pH from 7.4 to 4.6 and then back to 7.4 again. The images were taken from the same spot, but since the LNPs became more mobile upon pH changing, it may not look like the same LNPs in all images. Comparing these images of the LNPs with each other, it is evident that the LPNs have undergone structural changes and, as a result of this, the cargo has also been affected. In additional, these results indicate that permanent structural changes have occurred on the LNPs upon lowering the pH, and this finding was also in the QCM-D measurements, Figures (3.25) and (3.27).

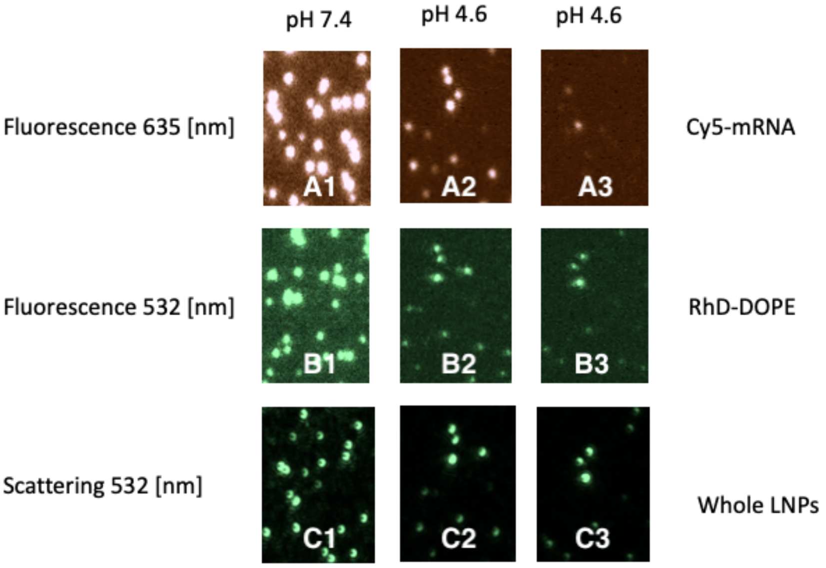

Figure 3.33: Waveguide microscopy measurements of the bound LNPs not preexposure to ApoE on SLB captured at different wavelengths and pH. The first column illustrate the bound LNPs at pH 7.6. The middle one is at pH-value 4.6, and then the column to the left shows when the pH-value of the LNPs had been increased back to pH of 7.4. The A-row show the fluorescence signal from the cargo. The B-row shows the fluorescence-labeled lipids in the LNPs (RhD-DOPE), and which is C-row shows the whole LNPs taken with scattering mode.

Moving to the next measurement, we lowered the pH in the experiment shown in Figure (3.19). Prior to lowering the pH in bulk, the bound LNPs that had been preexposed to the ApoE was further rinsed with PBS by pipetting. The results are shown in a scatter plot in Figure (3.34). The scatter plot of the bound LNPs that had been preexposed to ApoE shows that both scattering and fluorescence intensity upon the pH lowering was decreased, but not as much as in the case when the LNPs was not pre-exposed to ApoE, Figure (3.28). This observation indicates that LNPs without preexposure to ApoE were more sensitive when the pH was lowered. This behavior has also been indicated in our QCM-D measurements, where LNPs without ApoE had larger structural changes.

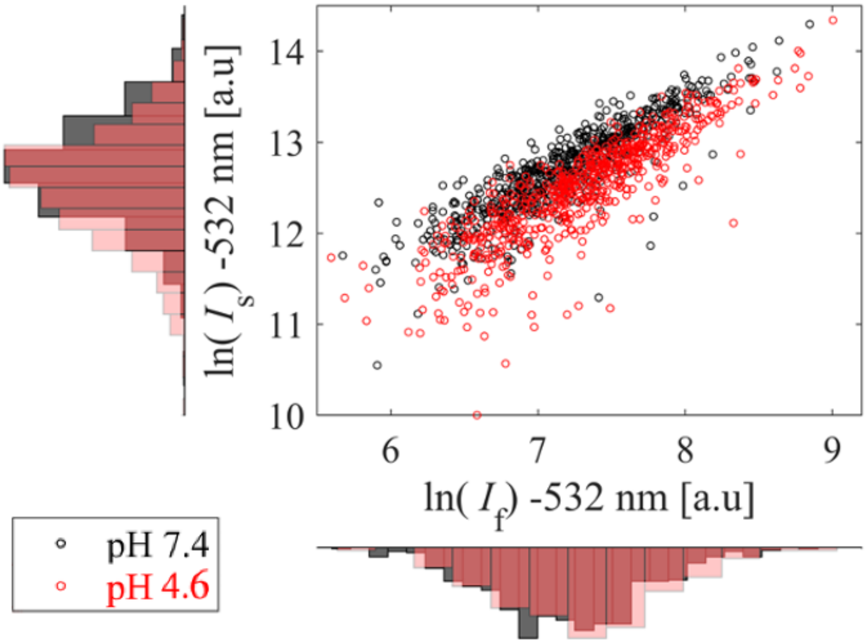

Figure 3.34: Scatter plots from the log-log plot of the scattering signal (whole LNPs) versus the fluorescence signal (from RhD-DOPE) of the the bound LNPs preexposure to ApoE at pH 7.4 (black histogram and circles) and pH 4.6 (red histogram and circles), at wavelength 532 nm

The micrographs in Figure (3.35) show the LNPs before, during, and after pH was lowered in the system. As it can be seen, the scattering signals that originate from the whole LNPs are almost unaffected during the experiments. The fluorescence signals from the cargo and the RhD-DOPE lipids were mostly affected by the change in the pH. These results indicate that the LNPs had interacted with the SLB but not as much as in the case when the LNPs were not preexposed to ApoE.

In addition, during the experiments, the LNPs had less mobility compared to the LNPs in an experiment where the LNPs were not diluted before the experiment and heated up to the body temperature. This difference in mobility might partially be due to the LNPs having undergone PEG-shedding, making them more charged and interacting with the SLB. Further, it might also be due to PEG-shedding, the LNPs had more contact points in the binding to the surface via biotin-SA.

However, in both results (3.18) and (3.34), decreasing intensity reveals that the LNPs have undergone some structural changes. In addition, comparing these results shows that the intensity in case where the LNPs were not pre-exposed to ApoE decreases more upon pH decreasing, which is also clear by comparing images in Figures (3.33) and (3.35).

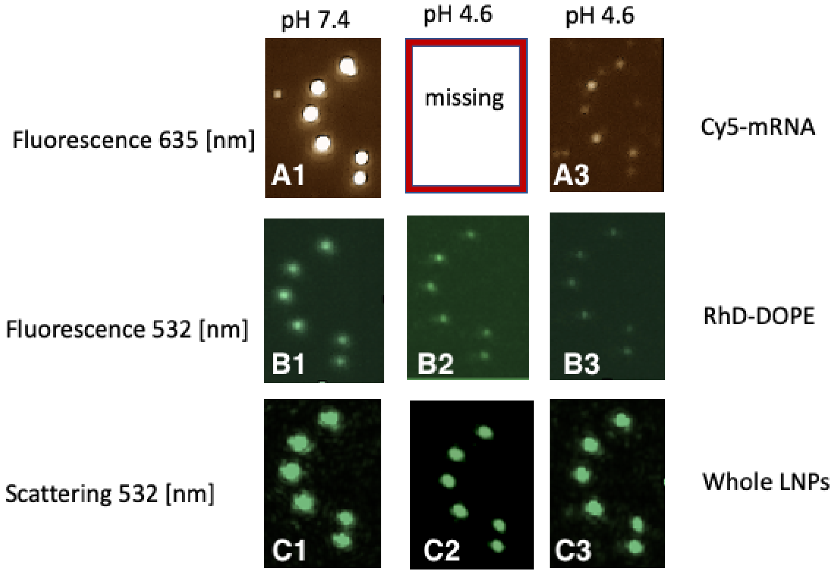

Figure 3.35: Waveguide microscopy measurements of the bound LNPs preexposure to ApoE on SLB captured at different wavelengths and pH. The first column illustrate the bound LNPs at pH 7.6. The middle one is at pH-value 4.6, and then the column to the left shows when the pH-value of the LNPs had been increased back to 7.4. The A-row show the fluorescence signal from the cargo. The B-row shows the fluorescence-labeled lipids in the LNPs (RhD-DOPE), and which is C-row shows the whole LNPs taken with scattering mode.

Furthermore, by analyzing the scatters plot in Figures (3.28), (3.34) and (3.36), thorough taking a log-log plot of the scattering signal versus the fluorescence signal, one can obtain a slope that gives information about the contents of the LNPs. This information may include if the length of the cargo is proportional to the size of the LNPs or to find out the qualitatively the location of the RhD-DOPE-lipids in the LNPs, such as if these lipids are inside or on the surface of the LNPs.

In this kind of analysis, we expected a slope of 2 for the cargo and 3 for RhD-DOPE-lipids. However, in our experiment, we obtain a slope of between 1-2 for both the cargo and RhD-DOPE-lipids. Putting together these label-free and fluorescence-based waveguide microscopy results suggests that the cargo is not proportional to the size of the LNPs and the RhD-DOPE-lipids are not only on the surfaces of the LNPs, which might be due to the self-assembly processes utilized for LNPs fabrication may vary with LNP size.

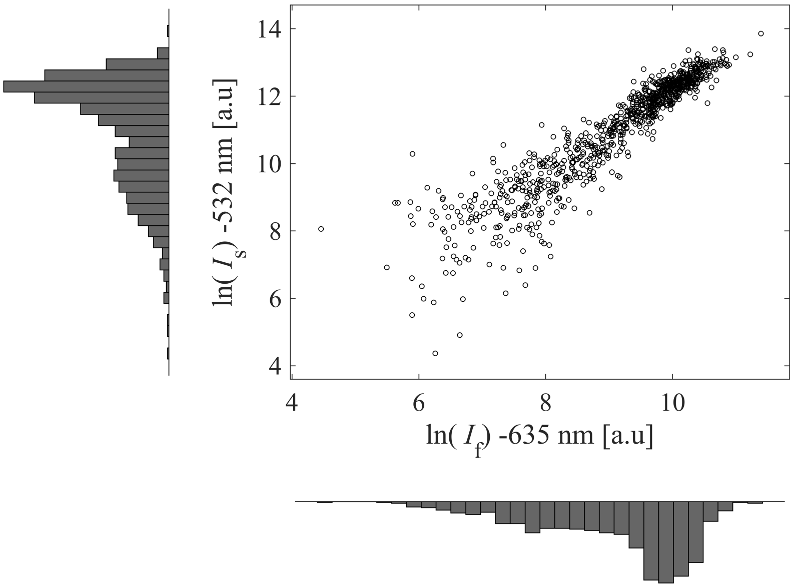

Figure 3.36: Scatter plots from the log-log plot of the scattering signal (whole LNPs) versus the fluorescence signal (from cargo) of the bound LNPs preexposure to ApoE at pH 7.4, prior lowering the pH, at wavelength 635 nm

It is worth mentioning that waveguide microscopy is a new technology, and therefore these experiments need to be further studied and analyzed. Moreover, several studies are also needed to further understand the structural changes of the LNPs upon the pH decreasing since our measurements indicate a clear difference in the structural changes of the LNPs with and without preexposure to the ApoE upon lowering the pH.

The primary aim of this section was to elucidate if any differences in structural changes of bare or protein covered LNPs upon a decreasing pH are detectable in the waveguide microscopy. Our results confirm that there are different structural changes on the LNPs depending on preexposure to ApoE. Furthermore, the results show that the cargo also is affected by structural changes. Further studies are needed to investigate the structural changes of the LNPs, especially when the cargo is affected by the structural change of the LNPs.

4

Conclusions & Future outlook

This chapter will summarise the main conclusions from each part of the results and discussions of this thesis, as well as including some suggestions for the future studies.

4.1 Lipid nanoparticles binding to the surface

Our QCM-D results showed that an SLB composed of the POPC and CAP-biotin is a good candidate for binding LNPs. Since LNPs bound easily to this surface, ApoE interacted irreversibly with the SLB, and the surface chemistry was almost unaffected by the varied pH. Through waveguide microscopy, we could further improve the quality of the SLB for the rest of the experiments by lowering the amount of CAP-biotin in the SLB. However, this surface chemistry can be improved more in future research by decreasing the amount of the CAP-Biotin, which might affect the reaction of the ApoE with the surface. Furthermore, one can compare the size distributions of the LNPs obtained from the NTA with the waveguide microscopy, which will reveal more details of the inhomogeneity of the LNPs production, which was not taken into account in this thesis. Waveguide microscopy can be used to monitor an event occurring on the surface in real-time via scattering and fluorescence modes, and it is an even more low-consuming technique than QCM-D.

4.2 Protein corona formation

ApoE seems to bind to LNPs, bound to an SLB via SA, with three kinetic phases, and the binding is flow rate dependent. The first binding phase is slower than the second one, possibly suggesting that PEG-shedding is occurring, while the third binding phase could perhaps be explained by aggregation of ApoE on the LNP surfaces. In order to investigate this speculation of the ApoE aggregations on LNPs, the protein solution of the ApoE mixed with bovine serum albumin (BSA) showed a monotone binding of the ApoE to the pre-bound LNPs. Furthermore, our studies showed that ApoE binds to PEG-modified LNPs with a lag-time of tens of minutes unless mixed with BSA. This is attributed to BSA-induced PEG-shedding, which promotes ApoE binding. There are many unanswered questions about the ApoE binding to the LNPs, such as: what is the mechanism behind the ApoE binding, how can a solution of ApoE mixed with BSA affect the ApoE binding to the LNPs, why ApoE is both temperature and flow rate dependent, how we can design LNPs that promote ApoE binding. Moreover, there is also need for a more detailed interpretation of the energy dissipation results of the QCM-D. In the future design of waveguide microscopy, one should take into account the flow rate setups.

4.3 Effect of a decreasing pH on bare and protein covered lipid nanoparticles

Our QCM-D results showed that, upon a pH decrease, the largest structural changes of the LNPs for both bare particles and those preexposed to ApoE is observed around pH 6. We have found that ApoE seems to dissociate from the preexposed LNPs at pH 4.6. More details about how much ApoE gets dissociated are needed in future studies. In addition, LNPs without preexposure to ApoE have different structural changes than the LNPs preexposure to ApoE, both in QCM-D and waveguide measurements. Furthermore, we have found that lowering pH induces a permanent structural change of the LNPs, affecting the escape of the cargo either into the SLB or in the bulk solution. Inspections using combined label-free and fluorescence-based waveguide microscopy releveled a weaker than expected dependence between cargo fluorescence and scattering intensity, suggesting that the self-assembly process utilized for LNPs fabrication may vary with LNPs size.

Bibliography

[1] Yáñez-Mó M, Siljander PRM, Andreu Z, Bedina Zavec A, Borràs FE, Buzas EI, et al. Biological properties of extracellular vesicles and their physiological functions. Journal of Extracellular Vesicles. 2015 Jan;4(1):27066.

[2] Grandin HM, Guillaume-Gentil O, Zambelli T, Mayer M, Houghtaling J, Palivan CG, et al. Bioinspired, nanoscale approaches in contemporary bioanalytics (Review). Biointerphases. 2018 Jul;13(4):040801.

[3] Roberts TC, Langer R, Wood MJA. Advances in oligonucleotide drug delivery. Nat Rev Drug Discovery. 2020 Oct;19:673–694.

[4] Wong KH, Riaz MK, Xie Y, Zhang X, Liu Q, Chen H, et al. Review of Current Strategies for Delivering Alzheimer's Disease Drugs across the Blood-Brain Barrier. Int J Mol Sci. 2019 Jan;20(2):381.

[5] Kim J, Basak JM, Holtzman DM. The role of apolipoprotein E in Alzheimer's disease. Neuron. 2009 Aug;63(3):287–303.

[6] Zhao R, Lu Z, Yang J, Zhang L, Li Y, Zhang X. Drug Delivery System in the Treatment of Diabetes Mellitus. Front Bioeng Biotechnol. 2020;8.

[7] Geldenhuys WJ, Khayat MT, Yun J, Nayeem MA. Drug Delivery and Nanoformulations for the Cardiovascular System. Res Rev Drug Deliv. 2017 Feb;1(1):32–40. Available from: `https://pubmed.ncbi.nlm.nih.gov/28713881`.

[8] Reverse Engineering the source code of the BioNTech/Pfizer SARS-CoV-2 Vaccine - Articles; 2020. [Online; accessed 22. May 2021]. Available from: `https://berthub.eu/articles/posts/reverse-engineering-source-code-of-the-biontech-pfizer-vaccine`.

[9] Grandin HM, Guillaume-Gentil O, Zambelli T, Mayer M, Houghtaling J, Palivan CG, et al. Bioinspired, nanoscale approaches in contemporary bioanalytics (Review). Biointerphases. 2018 Jul;13(4):040801.

[10] Springer Series in Biophysics;. Available from: `https://www.springer.com/series/835`.

[11] Yanez Arteta M, Kjellman T, Bartesaghi S, Wallin S, Wu X, Kvist AJ, et al. Successful reprogramming of cellular protein production through mRNA delivered by functionalized lipid nanoparticles. Proc Natl Acad Sci USA. 2018 Apr;115(15):E3351–E3360.

[12] Blanco E, Shen H, Ferrari M. Principles of nanoparticle design for overcoming biological barriers to drug delivery. Nat Biotechnol. 2015 Sep;33:941–951.

[13] Hajj KA, Whitehead KA. Tools for translation: non-viral materials for therapeutic mRNA delivery. Nat Rev Mater. 2017 Sep;2(17056):1–17.

[14] Weissman D. mRNA transcript therapy. Expert Rev Vaccines. 2015 Feb;14(2):265–281.

[15] Dowdy SF. Overcoming cellular barriers for RNA therapeutics. Nat Biotechnol. 2017 Mar;35:222–229.

[16] Difference Between mRNA Vaccine and Traditional Vaccine; 2021. [Online; accessed 25. May 2021]. Available from: `http://www.differencebetween.net/science/difference-between-mrna-vaccine-and-traditional-vaccine`.

[17] Walkey CD, Chan WCW. Understanding and controlling the interaction of nanomaterials with proteins in a physiological environment. Chem Soc Rev. 2012 Apr;41(7):2780–2799.

[18] Monopoli MP, Walczyk D, Campbell A, Elia G, Lynch I, Bombelli FB, et al. Physical-chemical aspects of protein corona: relevance to in vitro and in vivo biological impacts of nanoparticles. J Am Chem Soc. 2011 Mar;133(8):2525–2534.

[19] Karmali PP, Simberg D (2011) Interactions of nanoparticles with plasma proteins: implication on clearance and toxicity of drug delivery systems. Expert Opin Drug Deliv 8:343–357 - Sök på Google; 2021. [Online; accessed 22. May 2021]. Available from: `https://www.google.com/search?q=Karmali+PP`.

[20] Kaneva AM, Bojko ER, Potolitsyna NN, Odland JO. Plasma levels of apolipoprotein-E in residents of the European North of Russia. Lipids Health Dis. 2013 Dec;12(1):1–7.

[21] APOE (human); 2021. [Online; accessed 22. May 2021]. Available from: `https://www.phosphosite.org/proteinAction.action?id=8856&showAllSites=true`.

[22] Bittar R, Carrié A, Nouadje G, Cherfils C, Fesel-Fouquier V, Barbot-Trystram L, et al. Evaluation of a semi-automatic isoelectric focusing method for apolipoprotein E phenotyping. Practical Laboratory Medicine. 2020 Jan;18:e00150.

[23] Martínez-Morillo E, Hansson O, Atagi Y, Bu G, Minthon L, Diamandis EP, et al. Total apolipoprotein E levels and specific isoform composition in cerebrospinal fluid and plasma from Alzheimer's disease patients and controls. Acta Neuropathol. 2014 May;127(5):633–643.

[24] Vlasova IM, Saletsky AM. Study of the denaturation of human serum albumin by sodium dodecyl sulfate using the intrinsic fluorescence of albumin. J Appl Spectrosc. 2009 Jul;76(4):536–541.

[25] Purtell JN, Pesce AJ, Clyne DH, Miller WC, Pollak VE, Bramlage R, et al. Isoelectric point of albumin: Effect on renal handling of albumin. Kidney Int. 1979 Sep;16(3):366–376.

[26] Varkouhi AK, Scholte M, Storm G, Haisma HJ. Endosomal escape pathways for delivery of biologicals. J Control Release. 2011 May;151(3):220–228.

[27] Hu YB, Dammer EB, Ren RJ, Wang G. The endosomal-lysosomal system: from acidification and cargo sorting to neurodegeneration. Transl Neurodegener. 2015;4.

[28] Rodahl M, Höök F, Krozer A, Brzezinski P, Kasemo B. Quartz crystal microbalance setup for frequency and Q-factor measurements in gaseous and liquid environments. Rev Sci Instrum. 1995 Jul;66(7):3924–3930.

[29] Agnarsson B, Lundgren A, Gunnarsson A, Rabe M, Kunze A, Mapar M, et al. Evanescent Light-Scattering Microscopy for Label-Free Interfacial Imaging: From Single Sub-100 nm Vesicles to Live Cells. ACS Nano. 2015 Dec;9(12):11849–11862.

[30] Janshoff A, Galla HJ, Steinem C. Piezoelectric Mass-Sensing Devices as Biosensors-An Alternative to Optical Biosensors? Angew Chem Int Ed Engl. 2000 Nov;39(22):4004–4032.

[31] Cho NJ, Frank CW, Kasemo B, Höök F. Quartz crystal microbalance with dissipation monitoring of supported lipid bilayers on various substrates. Nat Protoc. 2010 Jun;5(6):1096–1106.

[32] Tymchenko N, Nilebäck E, Voinova MV, Gold J, Kasemo B, Svedhem S. Reversible changes in cell morphology due to cytoskeletal rearrangements measured in real-time by QCM-D. Biointerphases. 2012 Dec;7(1-4):43.

[33] Nilebäck E, Westberg F, Deinum J, Svedhem S. Viscoelastic Sensing of Conformational Changes in Plasminogen Induced upon Binding of Low Molecular Weight Compounds. Anal Chem. 2010 Oct;82(20):8374–8376.

[34] Dixon MC. Quartz Crystal Microbalance with Dissipation Monitoring: Enabling Real-Time Characterization of Biological Materials and Their Interactions. J Biomol Tech. 2008 Jul;19(3):151. Available from: `https://www.ncbi.nlm.nih.gov/pmc/articles/PMC2563918`.

[35] Sauerbrey, G. (1959) Verwendung von Schwingquarzen zur Wung dner Schichten und zur Mikrowung. Zeitschrift fur Physik, 155, 206-222. doi10.1007/BF01337937 - References - Scientific Research Publishing; 2021. [Online; accessed 22. May 2021]. Available from: `https://www.scirp.org/(S(351jmbntvnsjt1aadkposzje))/reference/ReferencesPapers.aspx?ReferenceID=126397`.

[36] Höök F, Kasemo B, Nylander T, Fant C, Sott K, Elwing H. Variations in Coupled Water, Viscoelastic Properties, and Film Thickness of a Mefp-1 Protein Film during Adsorption and Cross-Linking: A Quartz Crystal Microbalance with Dissipation Monitoring, Ellipsometry, and Surface Plasmon Resonance Study. Anal Chem. 2001 Dec;73(24):5796–5804.

[37] Sjöberg M, Mapar M, Armanious A, Zhdanov VP, Agnarsson B, Höök F. Time-Resolved and Label-Free Evanescent Light-Scattering Microscopy for Mass Quantification of Protein Binding to Single Lipid Vesicles. Nano Lett. 2021 May;2021.

[38] Docter D, Westmeier D, Markiewicz M, Stolte S, Knauer SK, Stauber RH. The nanoparticle biomolecule corona: lessons learned - challenge accepted? Chem Soc Rev. 2015 Oct;44(17):6094–6121.

[39] Sjöberg M. Characterization of biological nanoparticles using evanescent field sensing. Chalmers University of Technology; 2020. Available from: `https://research.chalmers.se/en/publication/518463`.

[40] Lakowicz JR. Principles of Fluorescence Spectroscopy. Springer-Verlag US: Springer US; 2006.

[41] González-González IM, Jaskolski F, Goldberg Y, Ashby MC, Henley JM. Measuring Membrane Protein Dynamics in Neurons Using Fluorescence Recovery

after Photobleach. In: Methods in Enzymology. vol. 504. Cambridge, MA, USA: Academic Press; 2012. p. 127–146.

[42] Huffman CFBR. Absorption and Scattering of Light by Small Particles; 1998.

[43] Kim A, Ng WB, Bernt W, Cho NJ. Validation of Size Estimation of Nanoparticle Tracking Analysis on Polydisperse Macromolecule Assembly. Sci Rep. 2019 Feb;9(2639):1–14.

[44] PLL-g-PEG Polymere - SuSoS; 2021. [Online; accessed 22. May 2021]. Available from: `https://susos.com/beschichtungstechnologien/pll-g-peg-polymere`.

[45] Jayapaul J, Schröder L. Molecular Sensing with Host Systems for Hyperpolarized 129Xe. Molecules. 2020 Oct;25(20).

[46] Nele V, Holme MN, Kauscher U, Thomas MR, Doutch JJ, Stevens MM. Effect of Formulation Method, Lipid Composition, and PEGylation on Vesicle Lamellarity: A Small-Angle Neutron Scattering Study. Langmuir. 2019 May;35(18):6064–6074.

DEPARTMENT OF SOME SUBJECT OR TECHNOLOGY
CHALMERS UNIVERSITY OF TECHNOLOGY
Gothenburg, Sweden
www.chalmers.se

CHALMERS
UNIVERSITY OF TECHNOLOGY